From Episodic Avalanching to Continuous Flow in a Granular Drum

N. J. Balmforth[1] **& J. N. McElwaine**[2]

[1] Department of Mathematics, University of British Columbia, Vancouver, BC V6T 1Z2, Canada

[2]Department of Earth Sciences, University of Durham, Durham, DH1 3LE, UK.

(Received 10 February 2017)

Experiments are conducted to study the transition from episodic avalanching (slumping) to continuous flow (rolling) in drums half full of granular material. The width and radius of the drum is varied and different granular materials are used, ranging from glass spheres with different radii to irregularly shaped sand. Image processing is performed in real time to extract relatively long time series of the surface slope derived from a linear fit to the granular surface. For the drums with glass spheres, the transition mostly takes the form of a blend of the characteristics of episodic avalanching and continuous flow, that gradually switches from slumping to rolling as the rotation rate increases. For sand, a hysteretic transition can be observed in which one observes prolonged episodic avalanching or continuous flow at the same rotation rate, spanning a window of rotation speeds. For drums with the smallest spheres (1 mm diameter), the transition takes the form of noise-driven intermittent switching between clearly identifiable phases of episodic avalanching or continuous flow. This style of transition is also found for the sand in either the largest or smallest drum (by volume). We formulate dimensionless groupings of the experimental parameters to locate the transition and characterize the mean surface slope and its fluctuations. We extract statistics for episodic avalanching, including angle distributions for avalanche initiation and cessation, the correlations between successive collapses, mean avalanche profiles and durations, and characteristic frequencies and spectra.

1. Introduction

The flow of grains in a horizontally rotating drum is one of the simplest experiments to perform, yet exemplifies most of the key features that complicate the dynamics of a granular medium (Caponeri *et al.* 1995; Mellmann 2001): as the drum rotates, phases of solid-like behaviour can co-exist with liquid-like or gas-like phases or be transformed into them. Even when the mean flow field is steady, particles can traverse yield surfaces to become entrained into flow or deposited into a solid bed. Finally, flow can abruptly halt or begin at different moments in time to furnish extensive intermittent motion. Thus, the rotating drum is perhaps the archetypal granular experiment.

If a theory existed that described the drum dynamics over all physical conditions, then one might consider that granular media flow problems had been solved. However, despite decades of study, most aspects of drum flow cannot be explained by any one model. For example, continuum models based on empirical friction laws (Forterre & Pouliquen

2008) or kinetic theory (Jenkins & Berzi 2010) chiefly apply to steady or rapid flow conditions and do not describe all the dynamics when there are transitions from solid-like to fluid-like behaviour. Worse, the literature on drum dynamics contains a number of overly simplistic or inaccurate theories and a variety of conflicting observations and interpretations, painting a poorly quantified picture of one of the more fundamental granular flow configurations. A first step to remedy this situation is to obtain reliable, reproducible and accurate experimental data, exploiting the continuous operation and image processing ability of modern cameras and computers to generate long stationary time series and high-quality statistics.

For a roughened cylinder, for which the granular material is unable to slide freely over the container, the low-speed flows are popularly classified as either "slumping" or "rolling" (Henein *et al.* 1983*a*; Mellmann 2001). The former consists of intervals of solid-body rotation that are interrupted by episodic avalanches and arises at the lowest rotation rates. The continuous steady flow of the rolling state emerges at higher rotation speeds. For both states of motion, the granular surface often remains relatively flat and is well characterized by a "dynamic friction angle"; there is only ever a shallow superficial flowing layer, bordered from the rigidly rotating grains below by a yield surface. At yet higher rotation rates, the surface profile becomes nonlinear, with a characteristic S-shape; eventually, rapid, gas-like flow emerges associated with significant centrifuging.

The transition between episodic avalanching and continuous flow has been documented to depend on particle diameter (relative to drum diameter) and shape, the aspect ratio and fill fraction of the drum, and effective gravity (Henein *et al.* 1983*a*; Ding *et al.* 2002; Liu *et al.* 2005; Brucks *et al.* 2007). Several studies have attempted to qualitatively describe the transition in terms of the matching of two distinct timescales. For example, Henein *et al.* (1983*b*) and Mellmann (2001) argue that the transition occurs when the typical duration of an avalanche matches the time taken for the same amount of material to rotate rigidly through a comparable angular change. This criterion has some empirical support, as do some other qualitative criteria (Ding *et al.* 2002; Rajchenbach 1990, 2002; Lim *et al.* 2003). However, none of these conditions emerge as the prediction of a dynamical theoretical model, nor do these studies address the precise form of the transition as a bifurcation in dynamical behaviour. Indeed, experimental studies often report a "transitional regime," wherein the flow mixes characteristics of both episodic avalanching and continuous flow, but offer no quantitative details (*e.g.* Henein *et al.* (1983*a*); Davidson *et al.* (2000); see also Brucks *et al.* (2007)).

By contrast, it has also been stated that the transition has a hysteretic form (Rajchenbach 1990): as one increases the drum rotation rate, episodic avalanching persists up to a threshold, before switching abruptly to continuous flow. If one then lowers the rotation rate, the continuous flow regime only becomes interrupted by episodic avalanching at a second, somewhat lower threshold. Both flow states are possible over the window of rotation rates sandwiched between the two thresholds. This description is rather different from a dynamical melange of slumping and rolling.

Most recently Fischer *et al.* (2009) have suggested that the transition is noise-driven, presenting detailed experimental observations in support of a "bifurcation by intermittency." In this scenario, there are again two co-existing states, but noise disrupts episodic avalanching at the higher rotation rates and terminates continuous flow at low speeds.

Over the window of the transition, the two states remain distinct and clearly identifiable, but stochastic fluctuations prompt intermittent switches between them. It is not clear whether the mix of behaviour reported in other studies corresponds to this intermittent switching, or whether the system dynamics is rougher, with no clear division into recognisable prolonged states of episodic avalanching or continuous flow.

A complementary theoretical approach is based on modelling the avalanching granular medium as a fluid-like continuum accelerating under gravity but retarded by solid-like friction (Caponeri *et al.* 1995; Rajchenbach 2000). The crudest models describe the dynamics in terms of a single evolution equation for the surface angle $\theta(t)$, allowing for switches in flow in the manner of a stick-slip friction law. When static friction is higher than dynamic friction at the initiation of flow, and if the latter then increases with flow rate (as in traditional Bagnold-type friction laws), the models predict two possible flow states at low rotation rates: a periodic stick-slip-type motion reproducing the episodic avalanching state, and a steady state representing continuous flow. As one increases the rotation rate, the periodic stick-slip solution eventually disappears in a deterministic bifurcation, with the system then converging to the rolling state. The critical rotation rate at which the periodic oscillations disappear offers a rationalization of the transition from slumping to rolling. Moreover, the presence of two co-existing states at lower rotation speeds implies pronounced hysteresis. However, the continuous flow state exists for arbitrarily low rotation rates and there is no transition from rolling to slumping. This can be remedied by destabilising the steady state in another deterministic bifurcation at low rotation rates by forcing the friction to start decreasing with flow speed (Caponeri *et al.* 1995; Rajchenbach 2000). Alternatively, noise can be added to the model to account for fluctuations due to the finite-size, granular nature of the medium. One can then disrupt the continuous flow state at lower rotation rate and episodic avalanching at higher rotation rates without passing through any deterministic bifurcations, and progress from a system showing pronounced hysteresis to one with an intermittent transition by raising the noise level (Fischer *et al.* 2009).

In the current paper, we provide an experimental exploration of slumping and rolling and the transition between the two, examining in detail the effect of drum and particle geometry. We summarize the details of the experiment in §2, and then describe our results for glass spheres (§3) and sand (§4). The Appendices (provided as supplementary material) contain some further technical details of the experiments, and a collection of additional results that back up our conclusions or provide extra information, but which we omit to streamline the main body of the paper.

2. The experiment

2.1. *Apparatus*

Our experiments were conducted using drums made from two acrylic cylinders fitted with a transparent front plate and a paper-covered back wall. For each, the position of the back wall could be adjusted to vary the drum width W (axial length), and the inner cylindrical surface was covered with (60 grit) sandpaper to reduce any slip of the granular materials. Most of the experiments were conducted in the larger of the cylinders, with a diameter D of about 30 cm, which was rotated relatively precisely at a prescribed rate

Drum diameter (inner), D (mm)		287, 190, 152, 100		137
Drum widths, W (mm)		17, 31, 56, 110, 205		17, 31, 56, 86
Rotation rates, Ω (rad/sec)		0.004–1		0.01–1
Nominal particle diameter (mm)	Range (μm)	θ_1	$\langle\theta_{\rm start}\rangle \pm \sigma_{start}$	$\langle\theta_{\rm stop}\rangle \pm \sigma_{stop}$
Glass spheres				
1	783–1132	21.3	21.7 ± 0.1	20.9 ± 0.1
1.5	994–1483	24.7	25.4 ± 0.3	24.3 ± 0.2
2	1800–2200	25.4	26.1 ± 0.3	24.9 ± 0.2
3	2800–3200	26.5	27.6 ± 0.4	25.8 ± 0.3
5	4800–5200	28.0	29.8 ± 0.7	26.9 ± 0.5
10	9800–10300	30.5	33.7 ± 1.4	28.3 ± 1.2
16	15600–16500	33.4	37.7 ± 2.0	30.1 ± 1.6
Sand				
1	624–1335	36	38.7 ± 0.3	34.8 ± 0.4

TABLE 1. Dimensions of the drums, their ranges of rotation rate, and the particle diameters and characteristic angles of the granular materials. The spheres with $d \leq 5$mm are produced by Potters Industries in a range of diameters and no further sieving was performed. The two larger spheres ($d = 10$ and 16mm) were commercial glass marbles for which we measured the diameter of spheres in representative samples directly with a caliper. Diameters less than 2 mm were measured in a Beckman Coulter LS13320 Laser Diffraction Particle Size Analyser, which precisely measures the distribution. The size range is given by d_{10}–d_{90} (the 10% and 90% percentiles, weighted by volume) for $d < 2$ mm and $d > 5$ mm; for $d = 2$ mm to 5 mm, we list the manufacturer's quoted size range. The characteristic angles are estimated using the largest drum ($D = 287$mm) with a width of $W = 110$mm; θ_1 is the surface angle at the commencement of continuous flow (§3.4); $\langle\theta_{\rm start}\rangle \pm \sigma_{start}$ and $\langle\theta_{\rm stop}\rangle \pm \sigma_{stop}$ are the mean starting and stopping angles during episodic avalanching, plus or minus their standard deviations (§ 3.5).

using friction rollers driven by a computer-controlled motor (see Appendix A). The front plate was made from glass. Cylindrical inserts with centring spacers were fabricated so that the diameter could be changed whilst using the same driving apparatus and data aquisition system. The smaller cylinder, with a diameter of about 14cm, had an acrylic front face and was mounted co-axially on a shaft driven directly by a geared-down motor. This second cylinder was used for a smaller number of more detailed measurements of the avalanching granular surface. Detailed measurements of the drums are provided in table 1.

To eliminate one of the experimental parameters, in all experiments the drum was half filled with the granular media (the "fill fraction" was 0.5). We used glass spheres for the most part, with the range of diameters listed in table 1. We also used a polydisperse sand with a diameter of about a millimetre. Table 1 reports some characteristic friction angles for these materials. It is conventional to determine such angles by building sandpiles or tilting a plane layer. However, the statistics for surface slopes are far better measured in the rotating drum. For example, in the episodic avalanching regime at low rotation speed, we can extract satisfying statistics for the angles at which avalanching begins ($\theta_{\rm start}$) and ends ($\theta_{\rm stop}$). These quantities are random-looking variables with well-defined

distributions; our measurements determine the mean values far more precisely than most existing sandpile experiments. One awkward issue is that these angles depend on drum width W and diameter D in our experiments (§3.4 and 3.5); table 1 quotes results for a relatively large drum with $D = 287\,\mathrm{mm}$ and $W = 110\,\mathrm{mm}$, for which at least the effect of the side walls is minimised. Mean angles of this type are also sensitive to ambient noise, dust and humidity. Indeed, a disturbing feature documented presently (§ 2.3) is a persistent ageing effect that leads to secular drifts of these angles as the drums rotate over long periods. Overall, despite their simple appeal, mean angle measurements of this sort are not robust measures of granular dynamics. We did not attempt to calibrate an empirical friction law like "$mu(I)$" using sheet flow down an inclined plane (GDR MiDi 2004).

The experiments were conducted in air-conditioned laboratories; the humidity was monitored to be $50 \pm 10\%$ over their duration. Although the humidity was not precisely controlled, once the granular materials were loaded inside the drums, the arrangement was well sealed and so humidity was unlikely to vary during each suite of experiments (*i.e.* the up-down sweeps described in § 2.3). The big drum was fixed to an optical table set on a workbench and which contained some vibration shielding. The smaller drum was mounted on a heavy wooden board. No further effort was made to reduce ambient noise, with other devices in the laboratory in operation during the experiments.

2.2. *Data analysis*

For each rotation rate, we used a video camera to record images of the granular medium through the front face of the drum. With a sampling rate of twenty or fewer frames per second, the images could be processed in real time, thereby avoiding the post-processing of excessive amounts of stored data. In particular, we used the contrast between the particles and the back (paper covered) wall to extract the location of the granular surface near the front glass face over a central section of the drum spanning about nine tenths of the total surface. The time series of the dynamical friction angle, $\theta(t)$, was then recorded exploiting a linear fit to the surface profile. Further details of the fitting process are summarized in Appendix A. For the 137 mm drum, we recorded movies of shorter duration and extracted the surface profile as a function of space and time.

In addition to the mean surface angle $\langle\theta\rangle$ (angular brackets denoting the time average), we also examine a number of other statistical measures extracted from the time series of $\theta(t)$, including the standard deviation of this signal, σ, and the distance skewness of its rate of change, D_{skew} (see Appendix A). The standard deviation highlights the strength of slumping, but also measures the unsteadiness of the flow during rolling. The distance skewness detects chiefly episodic avalanching: in this regime the time series of $\theta(t)$ contains rising portions at fixed rate punctuated by falling sections with variable rate, which translates to a highly skewed signal that registers strongly in the D_{skew} measurement.

For episodic avalanching, it is also insightful to record the starting and stopping angles of each collapse, θ_{start} and θ_{stop}, and the avalanche "amplitude" $\Delta\theta = \theta_{\mathrm{start}} - \theta_{\mathrm{stop}}$. Practically, the angles are determined by detecting all the local extrema in the time series that are separated in time and amplitude by preset thresholds. The thresholding artificially deletes some of the smaller avalanches from the record; we chose the thresh-

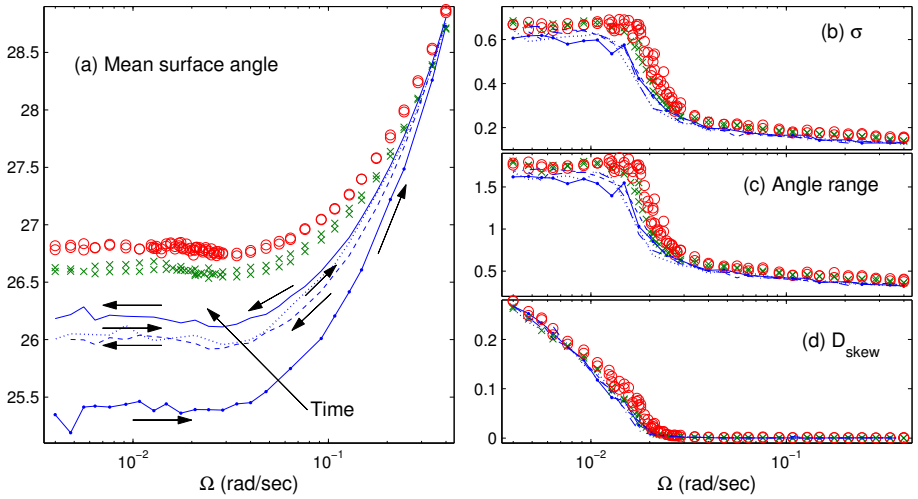

FIGURE 1. Repeated sweeps conducted with a fresh sample of 3 mm spheres in a drum with $(D, W) = (287, 110)$mm, showing (a) the secular increase of the mean surface angle $\langle\theta\rangle$, (b) the standard deviation σ of the surface angle time series, (c) the mean "avalanche amplitude" $\langle\Delta\theta\rangle = \langle\theta_{start} - \theta_{stop}\rangle$, and (d) D_{skew}, the optimised distance skewness of $\dot{\theta}(t)$. For the sweeps, the rotation rate is first stepped up (dots/solid line) and then stepped back down (dashed line); the up-down sequence is then repeated (dotted and solid lines). The circles and crosses show up-down sweeps for spheres aged according to our burn-in protocol.

olds to be as small as possible to avoid such deletions but avoid the false detection of events due to noise in the signal. The technical details are described in Appendix A. The procedure records data during the rolling regime, which do not correspond to "starting" and "stopping" angles. These measurements can still be useful as they provide another diagnostic of the fluctuations during continuous flow. In fact, for all our experiments, the mean avalanche amplitude $\langle\Delta\theta\rangle$ was closely related to σ (*cf.* figure 1(c)).

2.3. *Burn-in*

To explore the transition from episodic avalanching to continuous flow, we performed sequences of experiments corresponding to sweeps of rotation rate, holding fixed the other experimental parameters. For each sweep, Ω was incrementally raised and then lowered, waiting at each rotation rate for well over a hundred avalanches, identified either as the coherent collapses in the slumping regime or on the basis of individual particles during continuous flow. At all but the very lowest speeds the drum made at least one complete rotation. Short sections at the beginning of each time series were deleted to remove any transient adjustments occuring after the rotation rate was stepped up or down.

Unfortunately, at the outset of our exploration, a pronounced ageing effect became evident that made these sweeps problematic to conduct. The ageing corresponded to a gradual systematic drift in the mean surface angle, $\langle\theta\rangle$, that we attribute to a combination of accrued damage to the surfaces of the particles and the associated generation of fine dust. For the bigger particles, the surface damage and dust were visible to the eye (for $d = 16$ mm, the damage was substantial at the higher rotation rates, and we limited our use of this material); for the smaller particles, the surface damage was much less noticeable, even under a microscope. Sample secular changes are shown in figure 1 which

shows repeated up-down sweeps with $d = 3\,\mathrm{mm}$ glass spheres. Progressing from sweep to sweep, the mean angles gradually drift to higher values; the net change is dramatic, exceeding a degree.

For the larger glass spheres and sand, even though the mean angle drifted during the repeated sweeps, the other statistical measures of the signal, σ, $\langle \Delta\theta \rangle = \langle \theta_{\mathrm{start}} - \theta_{\mathrm{stop}} \rangle$ and D_{skew}, showed little or no such trend; see figure 1(b)–(d). Thus, despite the drift, several key features of the drum dynamics were robust, including the rotation rates characterising the transition between slumping and rolling. The transition, occuring for rotation rates near $\Omega \approx 2 \times 10^{-4}$ in the figure, is detected by the sharp change the diagnostics plotted in panels (b)–(d). By contrast, for the smaller spheres with $d \leq 1.5\,\mathrm{mm}$, the mean angle drifted to smaller values as the material aged and all the statistical measures also changed, with the rotation rates marking the transition shifting to lower values as the sweeps progressed. Most disconcertingly, after two up-down sweeps, the transition had migrated to such low rotation rate that episodic avalanching could barely be observed (see figure 31 in the supplementary material; hereon, we cite such figures using the superscript notation "Ⓢ31").

The drift of the mean angle could also be observed if the drum was rotated steadily at relatively high speed (0.4 rad/sec). In such experiments, the drift largely subsided after a characteristic "burn-in" time for all the particles[Ⓢ32]. This feature provided a convenient protocol for maturing particles to remove the problematic drift: starting with a fresh sample of particles, we first rotated the drum at constant, relatively high speed ($\Omega = 0.4\,\mathrm{rad/sec}$), monitoring the mean angle. Once any drift had subsided (which usually required many hours), we terminated this preliminary "burn-in" experiment and then conducted the up-down sweep in rotation rate. This ensured that there was minimal secular change between the rising and falling parts of the sweep, enabling us to look unambiguously for any other forms of hysteresis. Results from two sweeps with different batches of matured 3 mm spheres are included in figure 1; the elimination of the secular drift leaves discrepancies of order 0.1 degrees between the two batches that we attribute to basic experimental error (slight differences in the fill fraction of the drum, the fit of the surface slope, camera or drum positioning and so forth).

The pervasive effect on the surface angle associated with surface damage does not appear to have been reported in detail previously in the literature on rotating drums, although it is clearly connected to the industrial process of polishing. As our main effort was to explore the transition from episodic avalanching to continuous flow, we ignored the phenomenon once its main effects had been eliminated by the burn-in. However, although the protocol successfully yielded repeatable, consistent results for the larger spheres with $d > 1.5\,\mathrm{mm}$ and the sand, problems still remained for the smaller spheres. For $d = 1.5\,\mathrm{mm}$ spheres it turned out that one could remove the particles from the drum after the first burn, wash them, and then re-mature them in a second burn-in,[Ⓢ32] to obtain results that were reproducible and consistent with those for larger spheres. Unfortunately, for $d \leq 1\,\mathrm{mm}$, the maturation process still did not furnish results that we felt were sufficiently consistent and repeatable.[Ⓢ31] Consequently, below we report results chiefly for spheres with $d \geq 1.5\,\mathrm{mm}$.

To avoid repeating excessively long burn-in runs, we also recycled matured particles. In particular, we first matured particles in the drum with $(D, W) = (287, 110)\,\mathrm{mm}$, and then

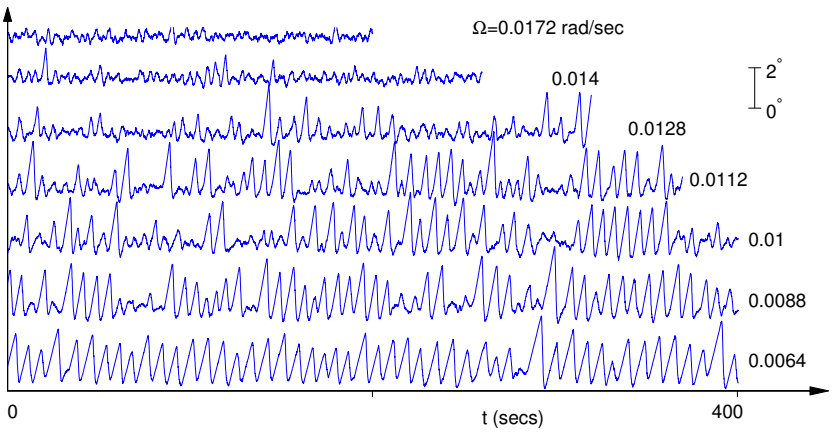

FIGURE 2. Sample time series of surface angle $\theta(t)$ for 2 mm spheres in the larger ($D = 287$ mm) drum, with $W = 31$ mm. Six time traces are shown (vertically offset), for the rotation rates indicated.

used the matured batches for all the subsequent sweeps in drums with different width and radius (see table 1). The recycled material still required some degree of burn-in (due perhaps to the loss of dust during removal and refilling of the drum), but typically less than half the time. The sandpaper lining the drums was also worn down by conducting repeated sweeps; we replaced the lining whenever wear became noticeable. No appreciable wear of the glass face of the drum was discernible.

3. The results for glass spheres

3.1. *Phenomenology*

We first discuss the basic avalanche dynamics of the glass spheres. Figure 2 displays sample time traces of the surface angle $\theta(t)$ for $d = 2$ mm and varying rotation rate in the drum with $(D, W) = (287, 31)$mm. At the larger rotations rates, the motion takes the form of unsteady continuous flow with angle fluctuations of order a tenth of a degree. As Ω decreases, sporadic larger-amplitude fluctuations arise, which are the signature of incipient episodic avalanches. At first, these fluctuations correspond to unsteady flow, with material never coming to rest. Lowering the rotation speed further, however, leads to the momentary arrest of flow and the emergence of genuine episodic avalanches. These events become more frequent and well developed as one lowers Ω still further, until they dominate the time series. At no stage is there an obvious alternation between prolonged, clear phases of either continuous flow or episodic avalanching. Hence there is a gradual transition from continuous flow to episodic avalanching, and there is no sign of any hysteresis if the rotation rate is varied up or down. This type of dynamics characterized all the spheres we used for the sweeps ($d \geq 1.5$mm); the melange of behaviour is likely responsible for the loose descriptions of the transition appearing in existing literature.

The transition for the smallest particles ($d = 1$ mm) took a rather clearer form, with much more obvious intermittent switching between clearly identifiable periods of episodic avalanching and continuous flow; see figure 3. Increasing the rotation rate through the transition, the typical residence time in the episodic avalanching gradually dwindled

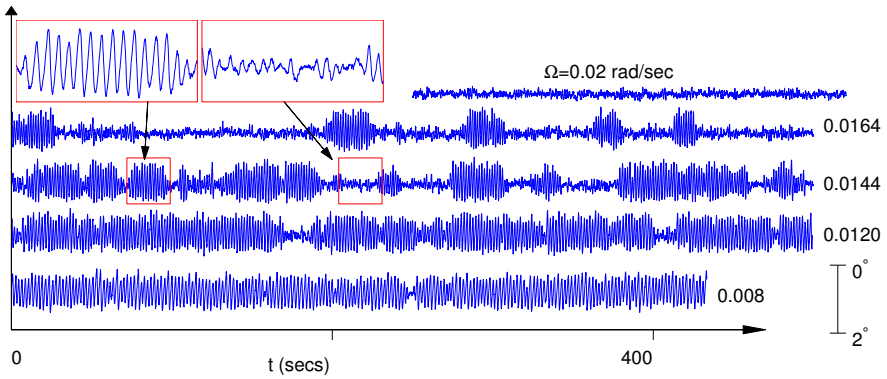

FIGURE 3. The intermittent transition for 1 mm spheres in the drum with $(D, W) = (289, 110)$mm.

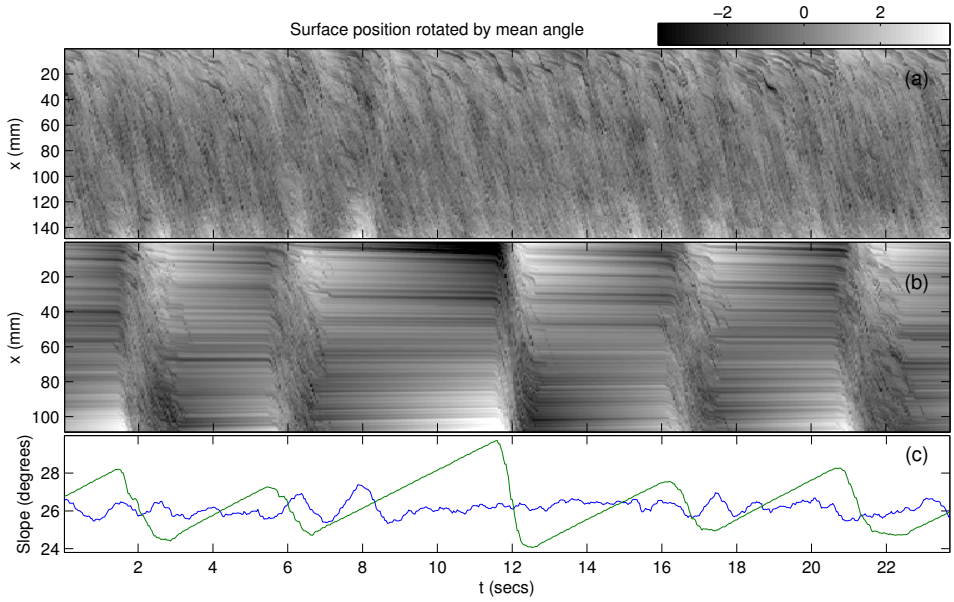

FIGURE 4. Two experiments in the smaller drum ($D = 137$ mm, $W = 31$ mm, $d = 2$ mm) for (a) $\Omega = 0.079$ rad/sec and (b) $\Omega = 0.019$ rad/sec. Panels (a) and (b) show the surface position (in mm) as a density on the space-time plane, after rotation by the mean angle. Panel (c) show the corresponding time series of surface angle $\theta(t)$.

until that state was replaced by uninterrupted continuous flow. Thus, for $d = 1$ mm the transition has a clear, "bursty" or intermittent character, as found by Fischer *et al.* (2009), with the residence time in the two phases providing a disgnostic of the transition. For the rest of the spheres, the time series displayed more a blend of behaviour than an irregular switching between two distinct states, suggestive of a higher degree of intrinsic noise in the dynamics. A residence time diagnostic was therefore difficult to extract, leading us to prefer σ and D_{skew}.

Figure 4 displays sample space-time plots of the surface position for $d = 2$mm spheres (less the short regions adjacent to the cylinder clipped from the base images) during

both continuous flow and episodic avalanching. The mean surface angle is subtracted off to emphasise the variations about that average. For the continuous flow, some residual coherent variations are still evident. For the episodic avalanches, it is difficult to isolate any particular position at which an avalanche begins or ends. On some occasions, the avalanche starts at end one end of the surface; on others, collapse occurs first at drum centre, or entire sections of the surface appear to mobilise simultaneously. Data collected from many avalanches suggested a weak bias of the starting position towards the top corner of the surface and the stopping position to the lower corner[S33].

3.2. *Sweeps*

Up-down sweeps of the glass spheres for different particle radius and drum geometry are shown in figure 5; the gradual transition between episodic avalanching and continuous flow leads to a smooth connection between $\Omega-$independent statistics for low rotations rates to more systematic variations at higher speeds. Figure 5(a) shows data for the drum with $(D, W) = (287, 110)$mm, and varying particle diameter d. Figures 5(b) and 5(c) show data for 3 mm spheres in drums with different diameter D and width W, respectively. These figures illustrate how the rotation rates characterizing transition vary significantly with D and d, but not with W. Both the mean angle and its variability depend significantly on all of D, W and d. Note the slight fall in the mean angle during the transition from slumping to rolling. In this figure, and in subsequent figures, each data point is an average over all experiments with the same parameters (Ω, d, D, W).

As illustrated by the lowest data in figure 5(c), the mean angles and standard deviations become independent of W once the drum is sufficiently wide. Such width-independent behaviour appears roughly for $W > \frac{1}{3}D$, independently of particle diameter and shape (being similar for all the glass spheres and sand), and in agreement with data presented by Courrech du Pont *et al.* (2003b). Many of the experimental drums used in previous studies are relatively narrow according to this criterion, with mean angles that are controlled by the side walls (Brucks *et al.* 2007; Félix *et al.* 2007; Orpe & Khakhar 2007). Despite this, the apparent independence of the flowing layer depth on W as observed through the side wall is sometimes taken as evidence for width-independent dynamics. Although we did not directly measure this depth, it was apparent from our image statistics (specifically, the mean difference between consecutive images, which highlights flowing rather than rigidly rotating particles) that the flowing layer also did not vary significantly with W at the front face of our drums. The situation is presumably similar to heap flows in a slot, for which Jop *et al.* (2005) argue that sidewall friction always controls the flowing layer depth and increases with W until the slot width becomes comparable to the length of the apparatus. Thus, observations through the sidewall must be biased, with the flowing layer being much deeper than can be seen, as has been verified in NMR experiments (Maneval *et al.* 2005).

Measuring mean angles through the front face of the drum can also be problematic, as surface slopes vary with axial position. For glass spheres, it has been reported that the surface angle changes by as much as 4°, with material piled up higher against the front and back walls (Dury *et al.* 1998). By itself, this variation is not sufficient to explain the differences in mean angle for different W observed for our drums (figure 5(c)). The characteristic range of the boundary effect is reported to be of the order of $0.14D$ by Dury

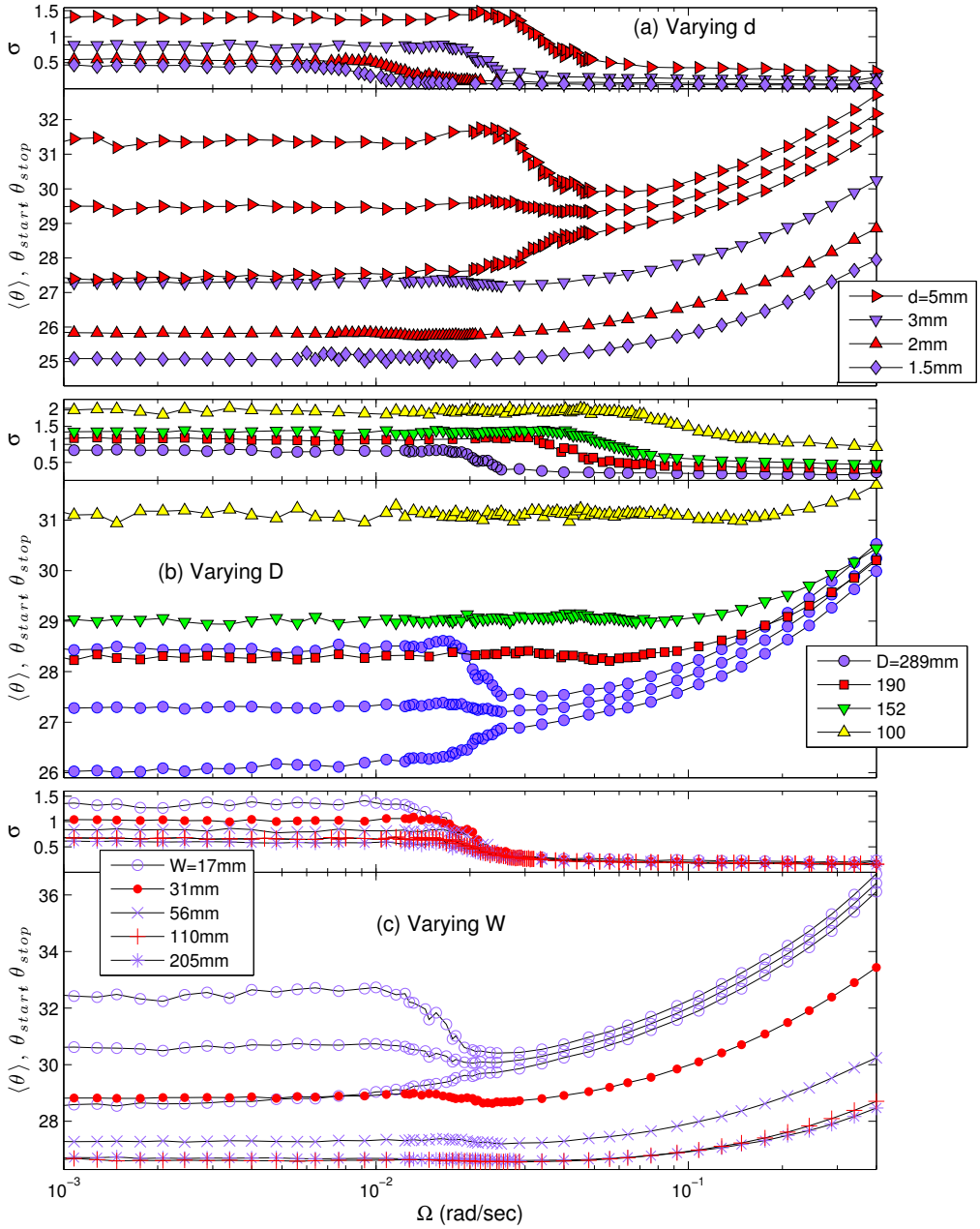

FIGURE 5. Mean surface angles $\langle\theta\rangle$ and standard deviation σ, against rotation rate Ω for glass spheres. (a) shows sweeps with the particle diameters indicated in the drum with diameter $D = 289\,\text{mm}$ and width $W = 56\,\text{mm}$. (b) shows sweeps for $d = 3\,\text{mm}$ in drums with $W = 56\text{mm}$ and the diameters D indicated. (c) shows sweeps for $d = 3\,\text{mm}$ in the drums with $D = 287\text{mm}$ and the widths W indicated. In each panel, the mean starting and stopping angles for one of the sweeps is also shown, and each data point is averaged over all experiments with the same (Ω, d, D, W).

et al., provided the particles are not too large. This suggests that the front and back wall are effectively isolated from one another when $W > 0.28D$, in agreement with our rough criterion $W > \frac{1}{3}D$. However, we made no attempt to quantify the axial variation of the surface slope in our drums.

3.3. *Locating the transition*

To locate the slumping-to-rolling transition more definitively, we use the diagnostics, D_{skew} and σ. These quantities are collected together for all the sweeps with glass spheres in figures 6 and 7.

The D_{skew} values in figure 6 can be used to locate the upper edge of the transition: we set $D_{skew} < D_{crit}$, with $D_{crit} = O(10^{-2})$, to indicate uninterrupted continuous flow. The upper edge of the transition is then given by $D_{skew} = D_{crit}$, which identifies a critical rotation rate Ω_c for each drum geometry and particle diameter. As shown by figure 6(a), with $D_{crit} = 0.02$, the critical rotation rates Ω_c spread over an order of magnitude and vary significantly with the ratio d/D of particle to drum diameter, but only very slightly with drum width. As shown in figure 6(b), the spread in Ω_c can be largely suppressed by formulating the scaled Froude number,

$$\mathrm{Fr}^* = \frac{\mathrm{Fr}}{1+\beta d/W}\left(\frac{D}{d}\right)^{\alpha}, \qquad \mathrm{Fr} = \Omega\sqrt{\frac{D}{g}}, \tag{3.1}$$

with $\alpha \approx 1.1$ and $\beta = 1.5$. The removal of drum-width dependence using the combination $\beta d/W$ is similar to previous adjustments of surface slope measurements (*e.g.* Courrech du Pont *et al.* 2003b; GDR-MiDi 2004), and is a device we exploit again below. With that factor in hand, the choice of α was then determined by a least squares fit. However, neither the inclusion of the factor $(1+\beta d/W)^{-1}$ with $\beta = 1.5$ nor the difference of the exponent α from unity are especially significant. In any event, we conclude that the upper edge of the transition is roughly given by $\mathrm{Fr} = \mathrm{Fr}^{upper}$, with

$$\frac{\mathrm{Fr}^{upper}}{1+bd/W}\left(\frac{D}{d}\right)^{\alpha} \approx \frac{1}{2}, \tag{3.2}$$

Note that the alignment of the transition by plotting D_{skew} against Ω/Ω_c in figure 6(b) does not collapse the entire set of sweep data onto a single curve: this diagnostic rises with rotation period for $\Omega < \Omega_c$ but spreads out due to an intrinsic dependence on drum width[§34], reflective of how episodic avalanching depend on W (see §3.5).

The lower edge of the transition is better highlighted by the standard deviation σ: this statistic becomes largely independent of rotation rate within the slumping regime; see figure 7(a). The data for episodic avalanching can be roughly collapsed by plotting $(\sigma - bd/W)(D/d)^c$ against $(D/d)^a\,\mathrm{Fr}$, with $a \approx 1.1$, $c \approx 0.9$ and $b = 4.5$. Given that the standard deviation is closely connected to $\langle\Delta\theta\rangle = \langle\theta_{\mathrm{start}} - \theta_{\mathrm{stop}}\rangle$ (roughly, $\langle\Delta\theta\rangle \approx 2.7\sigma$, with angle expressed in degrees), the collapse using $(\sigma - bd/W)(D/d)^c$ implies a pronounced dependence of the avalanche amplitude on the particle diameter and drum geometry. We expand further on this dependence in §3.5. For the moment we note only that the lower edge of the transition can be conveniently located by setting $\mathrm{Fr} = \mathrm{Fr}^{lower}$ with

$$\left(\frac{D}{d}\right)^{a}\mathrm{Fr}^{lower} = 0.3. \tag{3.3}$$

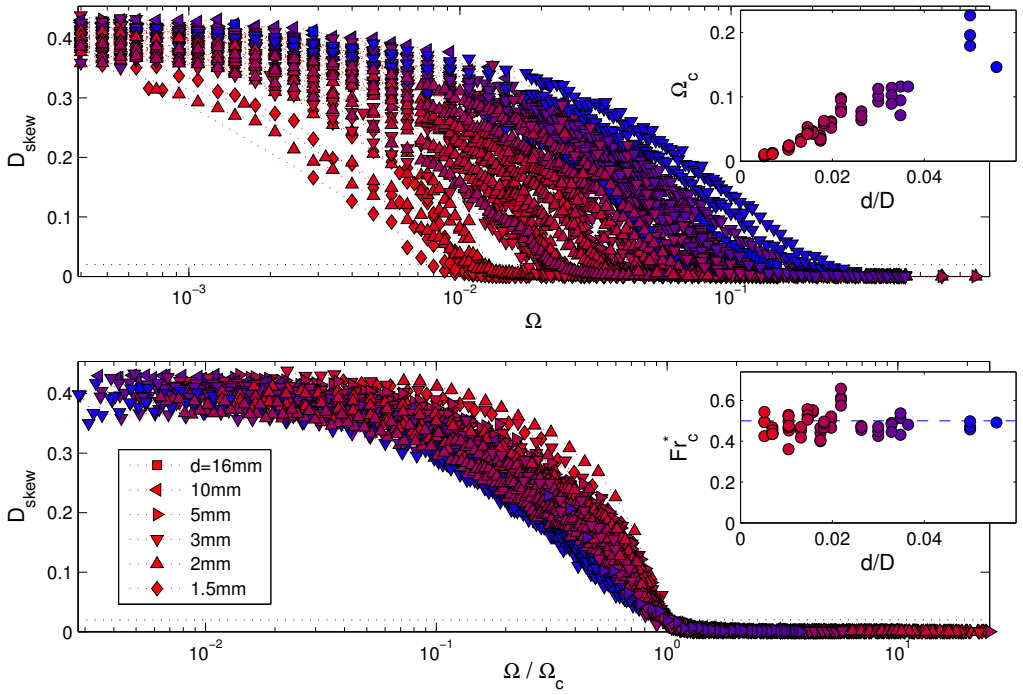

FIGURE 6. D_{skew} data for sweeps with spheres, with the symbol conventions for particle diameter d indicated. The data are plotted against (a) Ω and (b) Ω/Ω_c, where Ω_c is the critical rotation rate where $D_{skew} = D_{crit}$ for each sweep; here $D_{crit} = 0.02$ (dotted lines). The inset of (a) shows Ω_c against d/D. In the inset of (b), the critical rotation rates are scaled as Fr^* in (3.1) with $\alpha = 1.1$ and $\beta = 1.5$ (the dashed line shows $\mathrm{Fr}^* = \frac{1}{2}$). Symbols are colour coded from red to blue according to the value of d/D, as indicated in the inset.

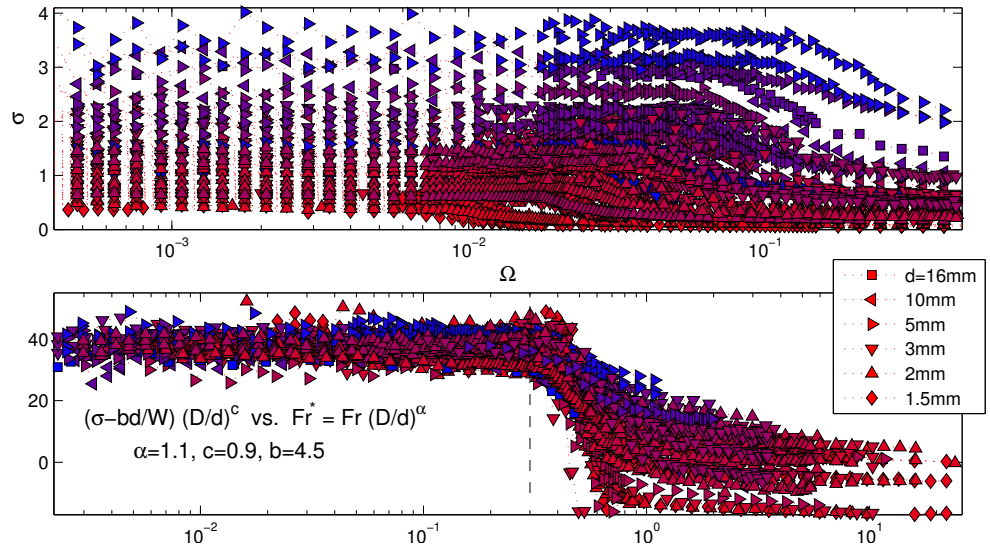

FIGURE 7. Standard deviation σ for sweeps with spheres, with the symbol conventions for d indicated. In (b), the data over the slumping regime is collapsed as indicated. Symbols are colour coded according to the value of d/D, as in figure 6.

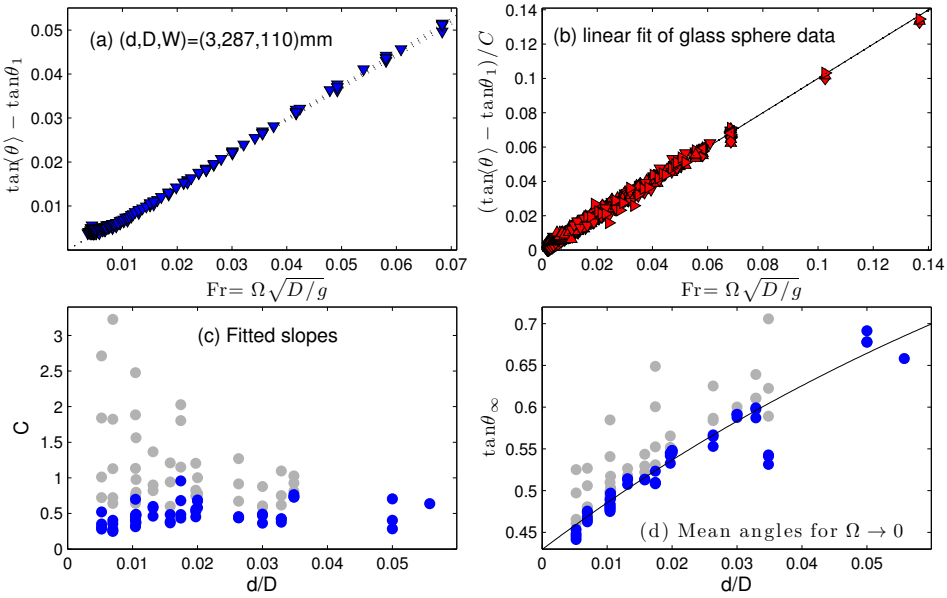

FIGURE 8. (a) Mean angles in continuous flow ($D_{skew} < 0.01$) for 3mm glass spheres in the drum with $(D, W) = (287, 110)$mm, plotting $\tan\langle\theta\rangle - \tan\theta_1$ against $\mathrm{Fr} = \Omega\sqrt{D/g}$, where $\tan\theta_1$ is the intercept of the linear fit (3.4) (dotted lines) for four different up-down sweeps. (b) Mean angles for all the glass sphere data, plotting $(\tan\langle\theta\rangle - \tan\theta_1)/C$ against Fr, where C is the slope of the linear fits, using the symbol conventions of figure 6. The fitting parameters C and $\tan\theta_1$ are plotted in grey in (c) and (d). For each, the additional fits in (3.5) are used to suppress the dependence on drum width; the adjusted values $(C, \tan\theta_1) - (\beta_C, \beta_1)d/W$ are plotted as the dark (blue) points. The parameters β_1 are plotted later in figure 11. In (d), the solid line shows the fit of $\frac{1}{2}(\tan\theta^\infty_{\rm start} + \tan\theta^\infty_{\rm stop})$ from figure 11.

Both (3.2) and (3.3) indicate that the transition migrates to zero rotation rate and disappears in the continuum limit ($d/D \to 0$). Neither criterion is completely consistent with estimates given in previous literature (Henein *et al.* 1983*b*; Mellmann 2001; Liu *et al.* 2005). Since the exponents α and a are not significantly different from unity, the estimates of Liu *et al.* (2005) show the same dependence on drum and particle diameter. These authors, however, also express the transition criteria in terms of the starting and stopping angles $\theta_{\rm start}$ and $\theta_{\rm stop}$, which they take to be material constants. In fact, these quantities depend on drum and particle geometry, as described in §3.5 and already documented in the literature (Courrech du Pont *et al.* 2003b; GDR-MiDi 2004).

3.4. *Continuous flow*

Mean surface slopes, $\tan\langle\theta\rangle$, during continuous flow are plotted in figure 8, first for a specific example ($d = 3$mm spheres in the drum with $(D, W) = (287, 110)$mm) and then for the whole data set of glass spheres. This figure illustrates that over the range of our experiments, the mean angle is well reproduced by the linear fit,

$$\tan\langle\theta\rangle \approx \tan\theta_1 + C\ \mathrm{Fr}. \tag{3.4}$$

For the $d = 3$mm spheres, the mean slope $\tan\langle\theta\rangle$ is plotted against Froude number, subtracting off the zero-Froude number limit, $\tan\theta_1$; a further scaling by the slope of

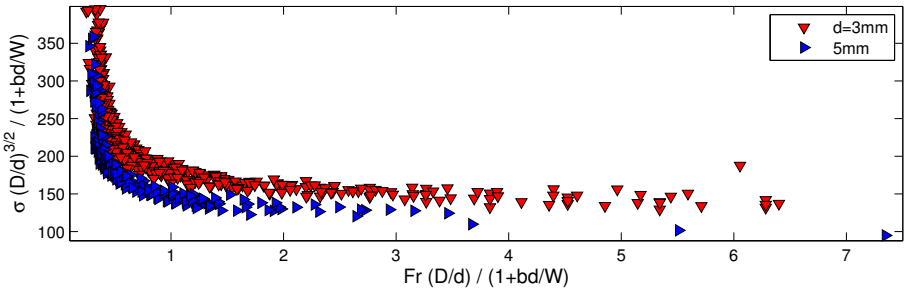

FIGURE 9. Standard deviations in the rolling regime ($D_{skew} < 0.01$) against Froude number, both scaled as indicated, for $d = 3$mm and 5mm. $b = 1.5$

the linear fit, C, is used in the plot for the entire data set. Here, the continuous flow regime is defined as $D_{skew} < D_{crit} = 0.01$, which is slightly smaller than in figure 6, but helps to ensure that all the data are above the transition; the choice leads to a minor improvement in fits to the data but is otherwise inconsequential.

Only at low rotation rates is there any discernible departure from (3.4), where the impending transition to episodic avalanching prompts the data to flatten out. Other than this feature, the mean slope data offer little warning of the transition, unlike what would be expected for a determinisitic bifurcation in dynamical behaviour. Indeed, the flattening of the mean slopes is consistent with the noise-driven emergence of incipient episodic avalanching which raises slope angles (see figure 2); if one were to artificially remove such events from the time series of $\theta(t)$, the mean surface slopes may well continue the linear trend to even lower rotation rate.

The intercepts, $\tan\theta_1$, and slopes, C, of the fits show some dependence on the drum diameter and width. We quote the values of θ_1 for $(D, W) = (287, 110)$ mm in table 1. As shown in the lower panels of figure 8, much of the dependence on drum width can be suppressed by using additional fits of the form,

$$C = C^{\infty} + \frac{\beta_C d}{W} \qquad \text{and} \qquad \tan\theta_1 = \tan\theta_1^{\infty} + \frac{\beta_1 d}{W}, \tag{3.5}$$

with parameters $(C^{\infty}, \theta_1^{\infty}, \beta_C, \beta_1)$. The adjusted mean slopes, $\tan\theta_1 - \beta_1 d/W$, vary in a clearer fashion with the ratio of particle to drum diameter, d/D (figure 8(c)). The adjusted parameters, $C - \beta_c d/W$, do not vary significantly with d/D; the remaining scatter in figure 8(d) more likely represents differences in surface properties or dispersivity between the different spheres.

Figure 9 shows an attempt to collapse the data for the standard deviation in the rolling regime. In particular, if we scale σ by $(D/d)^{3/2}/(1 + 3d/2W)$, there is a fair degree of collapse for the spheres with $d = 3$ mm and 5 mm. However, the scaling does not collapse the two sets of data, and works less well for other values of d. Figure 9 serves mainly to illustrate how the fluctuations in the rolling regime sharply increase as $\Omega \to 0$, suggesting that the continuous flow state inevitably becomes disrupted at low flow rates by noise, triggering the transition to episodic avalanching.

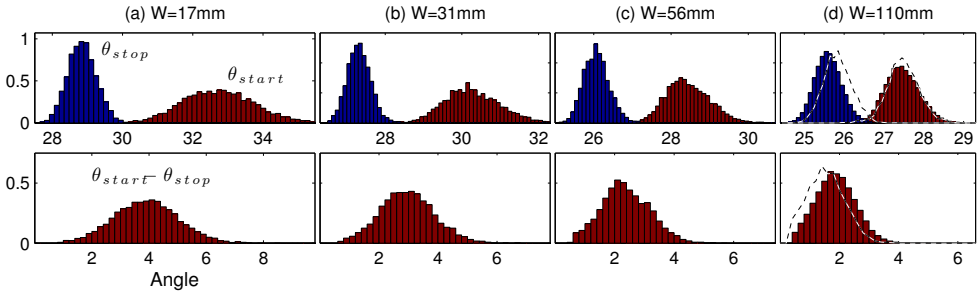

FIGURE 10. Histograms of the starting and stopping angles (top row), and the avalanche amplitude (bottom row) for $d = 3\,\mathrm{mm}$ glass spheres in the drum with $D = 287\mathrm{mm}$ in the episodic regime ($\Omega < 0.0092$), for the widths indicated. In the last panels for $W = 110\,\mathrm{mm}$, the dashed line shows the results for $W = 205\,\mathrm{mm}$.

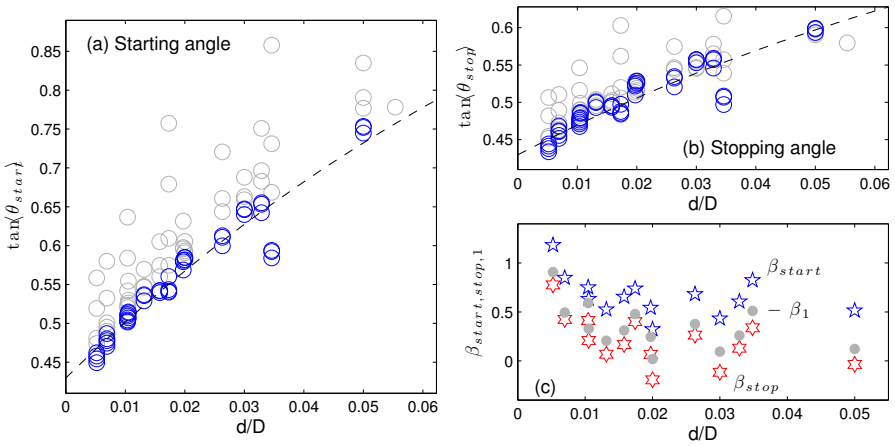

FIGURE 11. The median (a) starting and (b) stopping angles for glass spheres, averaged over the episodic regime ($\mathrm{Fr}(D/d)^a < 0.3$) and plotted in grey against d/D. For each d and D, the angles are fitted by $\tan\theta_{\mathrm{start,stop}} = \tan\theta^{\infty}_{\mathrm{start,stop}} + \beta_{\mathrm{start,stop}} d/W$; the extrapolations to infinite width, $\tan\theta_{\mathrm{start,stop}} - \beta_{\mathrm{start,stop}} d/W$, are then plotted in blue. The dashed line shows $a + b_{\mathrm{start,stop}}(e^{-\gamma d/D} - 1)$ where the parameters $(a, b_{\mathrm{start}}, \gamma)$ are chosen by a least-squares fit to the extrapolated starting angle data, and b_{stop} using a fit to the extrapolated stopping angle data. Panel (c) plots $\beta_{\mathrm{start,stop}}$ against d/D (blue pentagrams and red hexagrams); the grey dots are the fitting parameters β_1 from figure 8.

3.5. *Slumping statistics*

Statistics of episodic avalanching for the spheres are collected together in figures 10–12. The first picture displays histograms of the starting and stopping angles, and the avalanche amplitudes, $\Delta\theta = \theta_{start} - \theta_{stop}$, for $d = 3\,\mathrm{mm}$ in the drum with $D = 287\mathrm{mm}$ and varying width. Such angle histograms are largely independent of rotation rate,[§35] allowing the combination of all the data in the slumping regime. The histograms of θ_{start} and θ_{stop} appear Gaussian (cf. Fischer *et al.* 2008), although there are hints of skewness. Aside from a change in mean, the $\theta_{\mathrm{stop}}-$distribution appears to be independent of drum width.[§36(d)] In the widest drums, the $\theta_{\mathrm{start}}-$distribution is similar to that for θ_{stop}, but widens significantly as the drum narrows.[§36(c)] The starting and stopping angle distributions also do not remain separated but overlap in the wider drums, leading to an avalanche

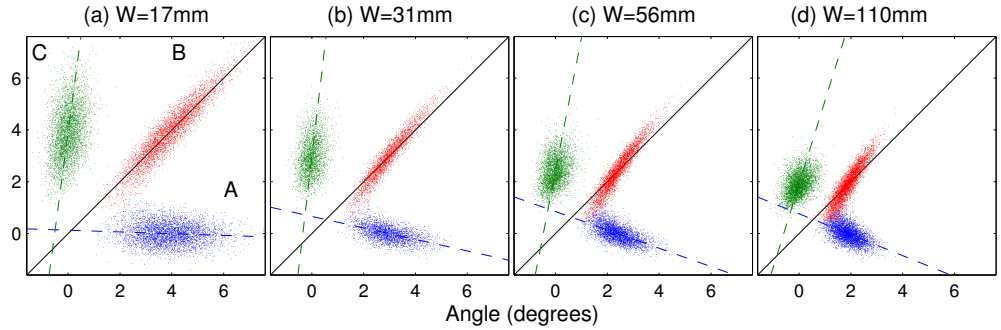

FIGURE 12. Scatter plots of starting and stopping angles for $d = 3$ mm spheres in drums with $D = 287$ mm and the widths indicated, taken over the entire episodic avalanching regime with $\Omega < 0.005$ rad/sec. In each case, three sets of data are shown: A plots $\theta_{\rm start} - \langle\theta_{\rm stop}\rangle$ against the subsequent $\theta_{\rm stop} - \langle\theta_{\rm stop}\rangle$; B denotes $\theta_{\rm start} - \langle\theta_{\rm stop}\rangle$ against the ensuing avalanche amplitude $\Delta\theta = \theta_{\rm start} - \theta_{\rm stop}$; C plots $\theta_{\rm start} - \langle\theta_{\rm stop}\rangle$ against the *preceding* $\theta_{\rm stop} - \langle\theta_{\rm stop}\rangle$. The dashed lines show least-squares linear fits to A and C, and the solid line is the diagonal.

amplitude distribution that falls linearly to zero amplitude for $\Delta\theta \to 0$,[Ⓢ36] allowing for the persistence of arbitrarily small avalanches (our algorithm for finding the extrema of the time series artificially eliminates the smallest avalanches in the histograms).

The wider spread in the starting angle distribution in the narrower drums reflects a greater variability in the strength of the spheres due to confinement and, as we show later, is much less prominent for sand. One interpretation of the variability in the bridging effect is that force chains appear for some packings and not others, and more often for spheres than for sand. Isolated stress supporting structures of this kind are perhaps more likely to inhibit the onset of flow rather than interrupt it, thus not impacting the stopping angle distribution.

Figure 11 displays the median values of the starting and stopping angles averaged across the episodic regime ($\mathrm{Fr}(D/d)^\alpha < 0.3$ with $\alpha = 1.1$). The width dependence of the angle data can again be largely suppressed using fits of the form,

$$\tan\theta_{\rm start,stop} = \tan\theta^\infty_{\rm start,stop} + \beta_{\rm start,stop}\frac{d}{W}. \tag{3.6}$$

The limiting angles $\theta^\infty_{\rm start,stop}$ depend on particle and drum diameter; fits to an exponential dependence on d/D are included in figure 11(a) and (b). The parameters, $\beta_{\rm start,stop}$, are plotted in figure 11(c) and are consistent with the fitting parameters β_1 used for the continuous flow data in figure 8 (which are also plotted), and values reported by Courrech du Pont *et al.* (2003*b*) and GDR MiDi (2004). Note that, over the episodic avalanching regime, the mean slope angle is equal to the average of the starting and stopping angles to less than one percent. The average of the limiting slopes, $\frac{1}{2}(\tan\theta^\infty_{\rm start} + \tan\theta^\infty_{\rm stop})$, is close to the extrapolation to zero Froude number of the mean angle during continuous flow (see figure 8).

Figure 12 presents "scatter" plots of the starting and stopping angles and the avalanche amplitude. The clearest feature of these plots is the tight connection between $\theta_{\rm start}$ and the ensuing amplitude $\Delta\theta = \theta_{\rm start} - \theta_{\rm stop}$ (data labelled B); *i.e.* for a given avalanche, the higher starting angle, the larger the avalanche (*cf.* Caponeri *et al.* 1990). As pointed out by Fischer *et al.* (2008), the data also suggest a weak negative correlation between

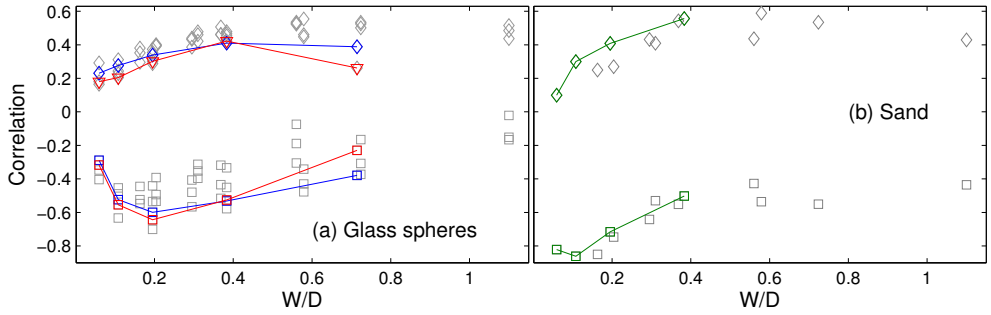

FIGURE 13. Correlation coefficients between $\theta_{\rm start}$ and the following $\theta_{\rm stop}$ (squares) and the previous $\theta_{\rm stop}$ (diamonds) plotted against W/D for (a) glass spheres and (b) sand, averaged over the episodic avalanching regime. In (a), the data for the big drum $D = 287$mm are connected by solid lines for $d = 2$mm (red) and 3mm (blue). In (b), the data for $D = 287$mm are connected by a (green) solid line.

$\theta_{\rm start}$ and the subsequent $\theta_{\rm stop}$ (data labelled A); the higher the start, the lower the stop. The weakness of this correlation implies that intrinsic noise and dissipation during flow are sufficient to wipe out much of the memory of the initiation of the avalanche.

Despite what is commonly assumed in the literature (e.g. Rajchenbach 2000), the plots also suggest a comparable correlation of $\theta_{\rm start}$ against the *previous* $\theta_{\rm stop}$. Indeed, as shown in figure 13, the magnitude of the average correlation of $\theta_{\rm start}$ with either the subsequent or previous $\theta_{\rm stop}$ is about 0.25 over the episodic range for the narrowest drums (the correlations are again largely independent of Ω in this regime[S37]). The correlations become stronger as the drum is widened, before falling off somewhat for the widest drums, perhaps because of the axial decorrelation of successive avalanches.

A correlation between $\theta_{\rm start}$ and the preceding $\theta_{\rm stop}$ is possible when the packing of material at the termination of an avalanche, reflecting to some degree the $\theta_{\rm stop}$, affects subsequent failure, *i.e.* $\theta_{\rm start}$. However, each avalanche uncovers fresh material in the upper parts of the drum, with a packing set by a much earlier collapse. Nevertheless, for spheres, failure does not always occur first at the top of the slope but can be elsewhere along the surface (§3.1), where the packing may have been set by the previous avalanche.

3.6. *Mean avalanche durations and profiles*

Figure 14 displays the mean avalanche duration, t_A, for glass spheres, defined as the average interval between the starting and stopping angles. This figure illustrates the curious result that the avalanche duration grows logarithmically as the rotation rate is decreased. There is also a modest but systematic dependence of t_A on drum width, which is for the most part consistent with the idea that sidewall friction slows and thereby prolongs avalanching.

The logarithmic growth of t_A with Ω disagrees with the results of Caponeri *et al.* (1995) and Fischer *et al.* (2008, 2009), who report avalanche durations that are independent of rotation rate. In agreement with these authors, however, the scaled avalanche duration $t_A\sqrt{D/g}$ does not vary strongly with drum or particle diameter. Caponeri *et al.* (1995) base their estimate of avalanche duration on the extrema of time series of the lower edge of the granular surface; given the nearly linear slope of the surface, this is similar to

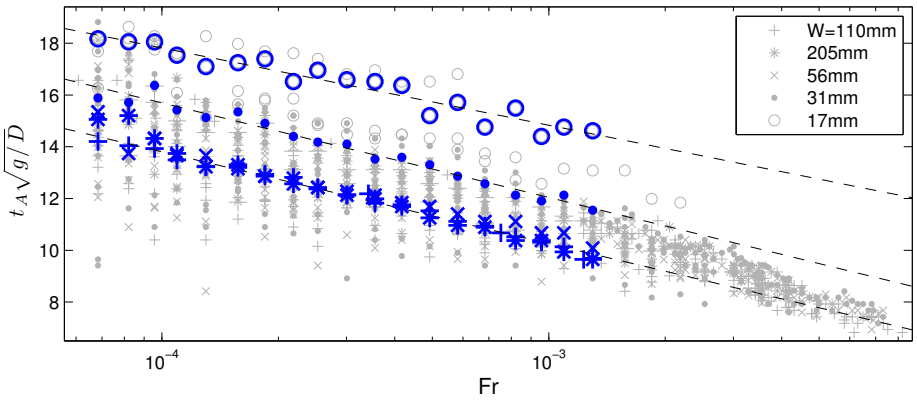

FIGURE 14. Scaled median avalanches durations $t_A\sqrt{g/D}$ against Fr for glass sphere data in the episodic regime (grey), with symbols corresponding to different drum widths as indicated. The dark (blue) symbols display 3 mm data for $D = 289$mm; the dashed lines are linear fits of $t_A\sqrt{g/D}$ with log Fr for the drums with $W = 110$ mm, 31 mm and 17 mm.

our measurement t_A. Fischer *et al.* (2008) estimate durations using a Gaussian fit to the profile of individual avalanches.

To understand this blend of agreement and disagreement, we examine the avalanche structure in more detail. Figure 15 shows the mean scaled avalanche profile, obtained by averaging, over all avalanches during a particular experiment, the time series of

$$\Phi(\tau) = \Phi(t - t_m) = \frac{\theta(t) - \theta_{\rm stop}}{\theta_{\rm start} - \theta_{\rm stop}}, \qquad \text{where } \theta(t_m) = \tfrac{1}{2}(\theta_{\rm start} + \theta_{\rm stop}). \tag{3.7}$$

This procedure suppresses the differences between avalanches, furnishing a smooth curve characteristic of the dynamics, much as found by Fischer *et al.* (2008). As shown in figure 15, the core of the profile remains largely unchanged as the rotation rate decreases. More significant is the change in the profile's maxima and minima, which become very flat and broad for low Ω, thereby lengthening the avalanche duration. In other words, t_A increases with rotation period because avalanches take longer to begin and end, not from a change in the time required for the surface angle to fall once motion is underway. The latter can be quantified by measuring $t_{1/2}$, the time required for $\Phi(t)$ to decrease from 3/4 to 1/4. This quantity is more comparable to the characteristic avalanche duration defined by Fischer *et al.*, and as shown in figure 15(d), varies far less significantly with Ω. Thus, different definitions are partly responsible for the disagreement in the rotation-rate dependence of the avalanche time. Note that, at the higher rotation rates, the mean avalanche profiles also display the preceding and ensuing avalanches, a feature resulting from a well-defined mean avalanche spacing (see below).

3.7. *Spectra*

In figure 16, we show power spectra for 3 mm spheres in the drum with $(D, W) = (287, 110)$ mm. At the lowest rotation rates (the top curves), there is a broad peak at an angular frequency ω that is a few hundred times Ω. The spectra level out at lower frequency, and then fall off algebraically at higher frequency, first with a dependence ω^{-2}, then steepening up to ω^{-4} and finally flattening off like ω^{-1}-noise. As one approaches

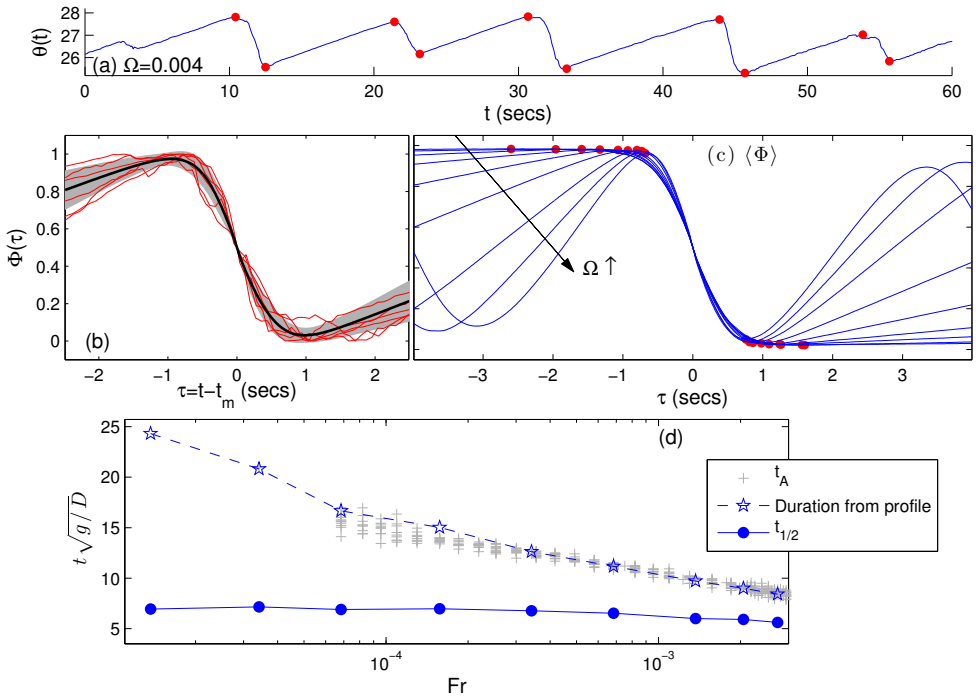

FIGURE 15. Avalanche structure for $(D, W) = (287, 110)$ mm and 3 mm spheres. (a) Time traces of surface angle at $\Omega = 0.004$ rad/sec, with the identified start and stop angles shown; the small avalanche near $t = 3$secs is not identified due to the clipping tolerances in the extremum search. (b) The mean scaled avalanche profile, obtained by averaging $\Phi(\tau = t - t_m)$ in (3.7). Also shown are six sample avalanches (red) and the mean plus or minus the standard deviation (shaded region). (c) Nine mean avalanche profiles for $W = 110$ mm at the rotation rates indicated in (d)); the maxima and minima are indicated. (d) The avalache duration defined as the time between the maximum and minimum of the mean scaled avalanche profiles. The characteristic time $t_{1/2}$ is also shown, as well as direct measurements of t_A (grey crosses).

the slumping-to-rolling transition, the dominant peak sharpens and its harmonic becomes visible. The peak almost disappears in the continuous flow regime, leaving a flat red spectrum that falls off algebraically at higher frequencies. The frequency of the dominant peak of the power spectrum is plotted against rotation rate in figure 17 for $(d, D) = (3, 287)$ mm and varying width.

The spectra are contaminated by additional peaks at the characteristic frequency ω_m of the stepper motor and some of its harmonics. These become visible at high rotation rate, occasionally taking over the dominant frequency. Further high-frequency peaks at $\omega_s = 8000\omega_m$ and its harmonics correspond to the steps of the motor. Although the extraneous peaks appear in the spectra, it is satisfying that they have a clear origin and there is no suggestion that they significantly influence the granular dynamics in general.

Over the episodic avalanching regime, most features of the power spectrum can be reproduced by the relatively simple stochastic model outlined in Appendix C. In brief, one assumes that the starting and stopping angles and the avalanche duration t_A are independent random variables (*i.e.* ignoring the correlations exposed in §3.5), and that the signal for the surface angle is composed of two linear pieces: a rise at rate Ω during

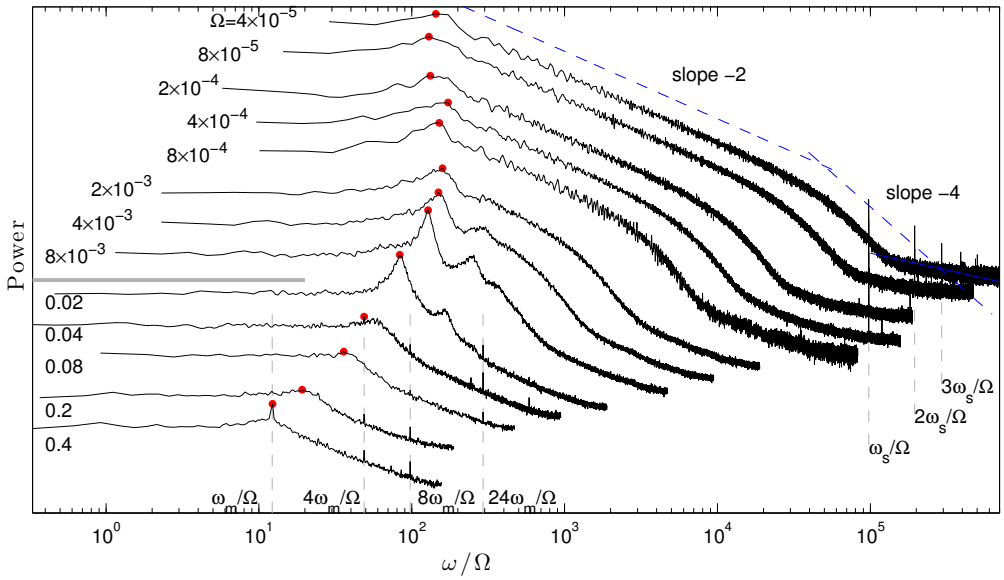

FIGURE 16. Power spectra for 3 mm spheres in the drum with $(D, W) = (287, 110)$ mm, plotted against ω/Ω for the rotation rates indicated, where ω is the angular frequency (in rad/sec). The spectra are offset for clarity and the dominant peak is identified. The vertical dashed lines show the additional frequencies ω_m, $\omega_s = 8000\omega_m$ and some of their harmonics. The transition is indicated by the grey horizontal line. The inclined dashed lines indicate slopes of -2 and -4.

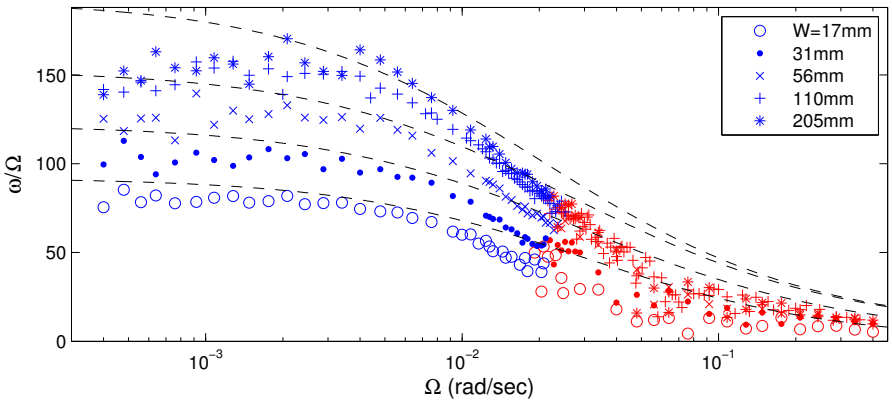

FIGURE 17. The frequency of the dominant peak in the power spectra for $d = 3$ mm spheres in the big drum with the widths indicated, plotting ω/Ω against $\log\Omega$. The blue (red) symbols indicate episodic avalanching (continuous flow). The dashed lines are the fits in (3.8) for $W \le 110$ mm.

solid-body rotation between $\theta_{\rm stop}$ and $\theta_{\rm start}$, then a linear collapse of duration t_A between $\theta_{\rm start}$ and the next $\theta_{\rm stop}$. The spectrum of this signal features a dominant frequency of

$$\omega_* = \frac{2\pi\Omega}{\langle \Delta\theta + \Omega t_A \rangle} \tag{3.8}$$

(cf. Davidson *et al.* 2000). This prediction is included in figure 17, using the linear fits of t_A with log Fr taken from figure 14.

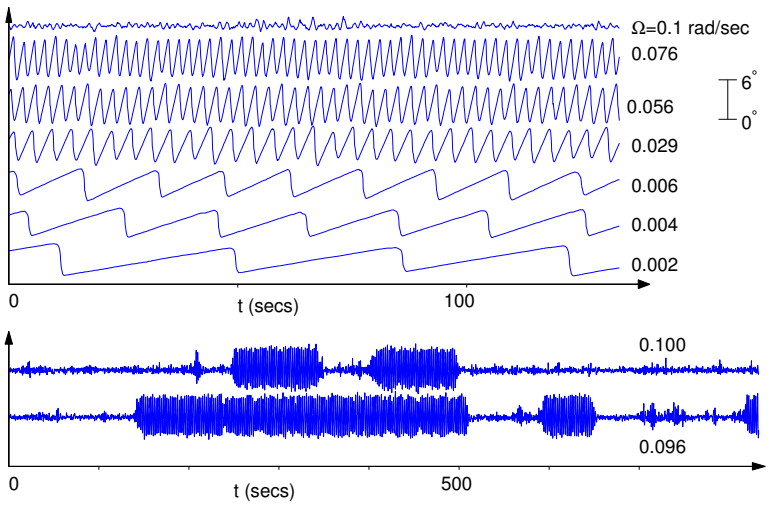

FIGURE 18. Sample time traces of $\theta(t)$ for the sand in the drum with $(D, W) = (287, 110)$ mm at the rotation rates indicated. The two time traces in the lower panel show intermittent behaviour over the transition.

In addition to the main peak, the spectrum of the synthetic signal is flat at low frequency, where the avalanches look like a random succession of impulses (cf. Caponeri *et al.* 1995). For $\omega_* \ll \omega \ll \langle t_A \rangle^{-1}$, the solid-body rise of the signal becomes resolved, but not the relatively rapid avalanches, so the signal resembles a sawtooth with the spectrum falling like ω^{-2}. Finally, for $\omega \gg t_A^{-1}$, the continuity of the signal over the avalanches is resolved and the spectrum then falls like ω^{-4}. With an avalanche duration of a few seconds (figure 14), the cross-over in the tail of the spectrum occurs for $\omega \sim t_A^{-1} \sim 1$ rad/sec, in rough agreement with the switch in scalings of the top curves in figure 16. The model also rationalizes the relation between the standard deviation of the surface angle and the avalanche amplitude: $\sigma^2 \approx \frac{1}{12}\langle \theta_{\rm start} - \theta_{\rm stop} \rangle^2 + \frac{1}{2}(\sigma^2_{\rm start} + \sigma^2_{\rm stop})$ when the avalanche duration is relatively small and $\sigma^2_{\rm start} - \sigma^2_{\rm stop} \ll \langle \Delta\theta \rangle^2$, where $\sigma_{\rm start}$ and $\sigma_{\rm stop}$ are the standard deviations of the starting and stopping angles.

4. Sand

4.1. *Avalanche phenomenology for sand*

To explore how the dynamics changes when we switch to aspherical particles, we performed up-down sweeps with sand. Sample time series of the surface angle for different rotation rate are shown in figure 18. The series display a much sharper switch in behaviour at the slumping-to-rolling transition than the spheres, and the episodic avalanching is much more regular, producing an almost periodic signal.

The space-time plots in figure 19 illustrate how the avalanche dynamics is quite different from the glass spheres: for sand, there are recognisable fronts that initiate and arrest flow, as remarked by Rajchenbach (2002). The first of these appears near the top end of the pile and propagates down to the lower end, activating the collapse. Once the advancing front reaches the bottom of the free surface, it triggers the retreating front which then propagates back up the surface to the upper end, switching off the flow. The

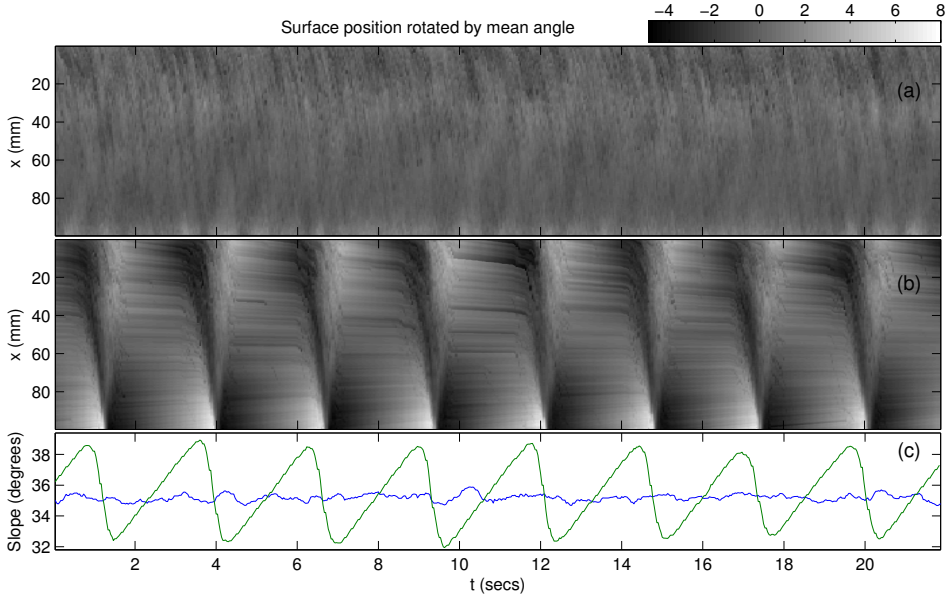

FIGURE 19. A similar picture to that in figure 4, but for the sand ($(D, W) = (137, 86)$ mm) with (a) $\Omega = 0.27$rad/sec and (b) $\Omega = 0.06$rad/sec.

starting and stopping positions of the avalanches are consequently always near the top corner of the granular surface[S33]. Neither front features in the dynamics of the spheres, as remarked by Fischer *et al.* (2008).

4.2. *Sweeps, intermittency and hysteresis*

For both the biggest and smallest drums with $(D, W) = (287, 110)$ and $(100, 31)$ mm a smooth transition with clear intermittent switching between phases of slumping and rolling is again evident (see the lower traces in figure 18 and the sweep data in figure 20(b)). However, for all the other drums the transition was different, occurring *via* a sudden jump from rolling to slumping or *vice versa*. Moreover, the jump from slumping to rolling occurred at higher rotation rates than the jump from rolling to slumping, leading to hysteresis in the sweep data; see figure 20(a). Note that multiple sweeps focusing on the transition are included in this figure; these demonstrate how the transitions between the two states do not occur at a single rotation rate but at seemingly random values of Ω spread over ranges that are narrower than the window of hysteresis.

A summary of the transitional Froude numbers for sand (as defined by $D_{skew} = 0.02$) is provided in figure 21, which plots the data against the volume ratio D^2W/d^3 and scales Fr as for the glass spheres in figure 6. The transition evidently occurs at rather higher rotation rates than predicted by (3.2). The scaling of the Froude number is also unable to align the data for either the intermittent drums or the two transitions bordering the region of hysteresis. Thus, the scalings observed for glass spheres do not work for sand. Partly responsible for this discrepancy is that the transition in sand depends significantly on drum width, unlike for spheres. This result is made more surprising by the fact that the statistics of rolling and slumping do not appear to depend significantly on the drum width (see below), again in contrast to spheres.

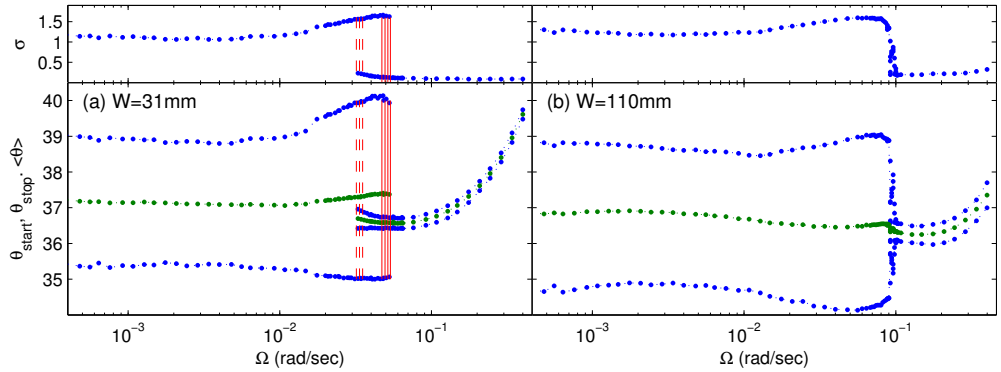

FIGURE 20. Up-down sweeps for sand in the big drum with $D = 289$mm, showing angle data and standard deviation plotted against Ω for the widths indicated. The sweeps include multiple repeated runs focusing around the transition; in (a) the switches between slumping to rolling arise for several rotation rates, as indicated by the vertical red dashed and solid lines (marking the switch to slumping or rolling, respectively). The data vary more strongly with Ω within the slumping regime than for spheres, at least for $\Omega > 0.01$, reflecting how the episodic avalanching occurs at higher rotation rates where drum speeds are no longer much smaller than flow speeds during an avalanche.

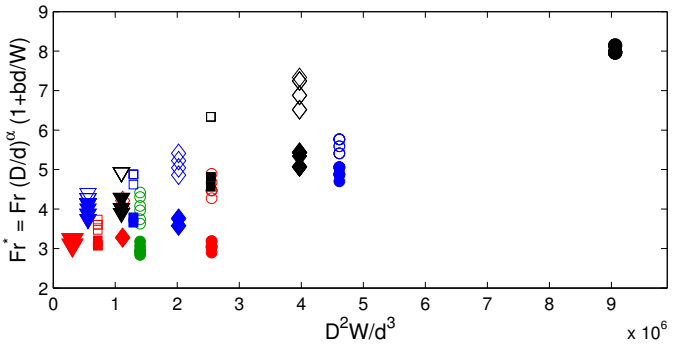

FIGURE 21. Scaled transition Froude numbers, $\mathrm{Fr}^* = \mathrm{Fr}(D/d)^\alpha(1+bd/W)$, against the volume ratio D^2W/d^3, for $\alpha = 1.1$ and $b = 1.5$ (see figure 6). Open (filled) symbols refer to the transition from slumping to rolling (rolling to slumping), with the conventions, $D = 289$mm - circles, 190mm - diamonds, 152mm - squares, and 100mm - triangles, and $W = 110$mm - black, 56mm - blue, 31mm - red, 17mm - green.

It is also not clear why the window of hysteresis opens in between our largest and smallest drums. Conceivably, enhanced fluctuations with fewer particles might wash out a hysteretic transition in the smallest drum; perhaps the opportunity for spatial decorrelation triggers additional perturbations and rationalises why the biggest drum also shows an intermittent transition. Either way, the window of hysteresis likely closes at these two extremes due to a reduction in the effective system noise.

Curiously, the mean angles for continuous flow in sand show a much more prominent upturn as one approaches transition. This is illustrated in figure 22, which plots the mean surface angles offset by the minimum slope and plotted against Froude number scaled by the value Fr_{min} where the minimum is attained. This way of plotting the data collapses much of the variation between the different drum geometries; the minimum

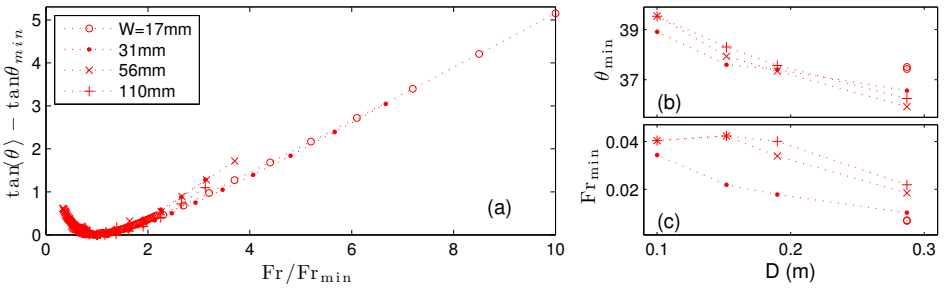

FIGURE 22. Mean slopes in the rolling regime for sand, plotting (a) $\tan\theta - \tan\theta_{min}$ against $\mathrm{Fr}/\,\mathrm{Fr}_{min}$, (b) $\tan\theta_{min}$ against D, and (c) Fr_{min} against D, with the symbol convention for drum width indicated.

slope depends on drum diameter but not obviously on its width, whereas Fr_{min} depends on both (see figure 22(b,c)). In the simple model of Caponeri *et al.* (1995) an upturn in the continuous flow solution arises from the non-monotonic dependence of the friction law, and destabilises that equilibrium to trigger the switch to slumping. No such instability is manifest in the experiments, with the upturn of the mean angle occupying a significant range of rotation rates characterized by robust continuous flow. This feature may explain Rajchenbach's (1990) observation that the mean angle increases like the square of the rotation rate, which is otherwise not supported by the data.

4.3. *Avalanche statistics and profiles for sand*

Figure 23 shows slumping statistics for sand; the corresponding starting-stopping-angle correlations are compared with results for glass spheres earlier in figure 13. Figure 23 illustrates how the dependence of the starting angle distribution on drum width is much less marked for sand. The irregular shape of this material allows particles to lock together more tightly in static arrangements in comparison to spheres; randomly appearing force chains bridging between the side walls may therefore be less likely to influence the dynamics. Moreover, in the wider drums, the starting and stopping angles remain well separated, furnishing a more Gaussian-like amplitude distribution that favours regular avalanching rather than collapses of arbitrarily low amplitude. The sand amplitude distribution is consequently sensitive to drum diameter but has no clear dependence on width[S38,39], unlike that for spheres.

The correlations between the starting and stopping angles are also different for sand (figure 13(b)). In the narrow drums, θ_{start} is poorly correlated with the previous θ_{stop}, consistent with the observation that the avalanches begin at the top of the drum, where fresh material has been exposed by the previous avalanche and the packing is relic from the distant past. The starting angle, however, is strongly negatively correlated with the subsequent stopping angle, and so dissipation and dynamical noise during flow cannot erase the memory of avalanche initiation. Widening the drum strengthens the correlation of θ_{start} with the preceding θ_{stop} whilst reducing its correlation with the subsequent θ_{stop}. In the widest drums, θ_{start} is roughly equally correlated with both (coefficients of about ± 0.5). Evidently, the wider drum features greater dynamical noise that suppresses the memory of initiation; the correlation with the previous start is less straightforward to understand.

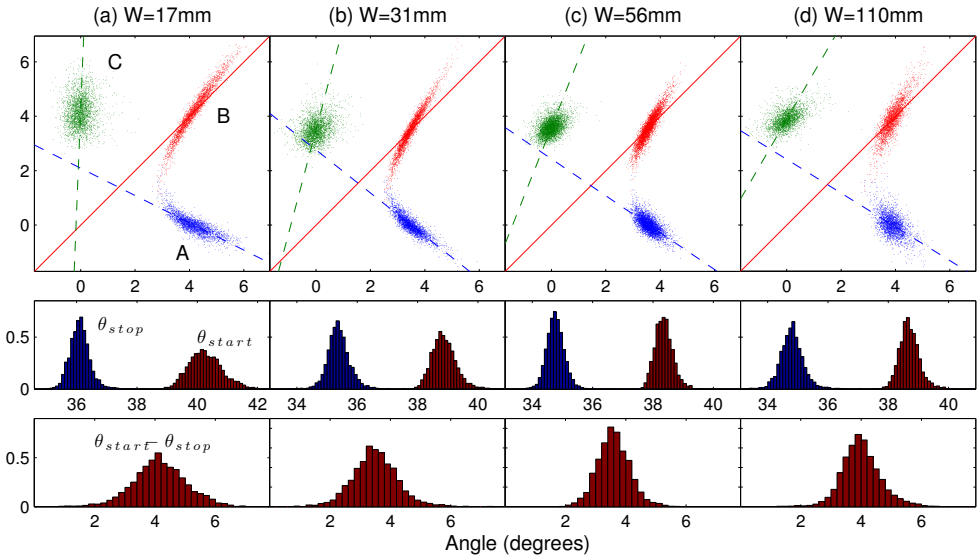

FIGURE 23. Avalanche statistics for sand in the drum with $D = 287\,\mathrm{mm}$ and the widths indicated, averaged over the episodic regime ($\Omega < 0.01$). Top row: scatter plot of $\theta_{\mathrm{start}} - \langle\theta_{\mathrm{stop}}\rangle$ against the following $\theta_{\mathrm{stop}} - \langle\theta_{\mathrm{stop}}\rangle$ (A; blue dots), the avalanche amplitude $\theta_{\mathrm{start}} - \theta_{\mathrm{stop}}$ (B; red dots), and the preceding $\theta_{\mathrm{stop}} - \langle\theta_{\mathrm{stop}}\rangle$ (C; green dots). The dashed lines show least-squares linear fits to A and C, and the solid line is the diagonal. Lower row: histograms of the starting and stopping angles.

Sample avalanche profiles for sand are shown in figure 24. Once again t_A increases logarithmically with rotation period due to the increasing time taken to initiate and terminate each avalanche. For wider drums, the time needed to start the avalanche dominates, whereas the time taken to end the event is more critical in narrower drums. The avalanche profiles contain more structure than their relatives for spheres (*cf.* figure 15). Most noticeable is the kink near the midpoint of the profile, which is caused by the two fronts that switch flow on and off: the kink occurs when the advancing front that mobilises flow reaches the bottom of the sand surface and reflects into the retreating front that arrests motion.

The preceding observations suggest a physical picture of sand avalanche dynamics: in the wider drums, the two fronts fully traverse the granular surface. The triggering front takes time to start at the lower rotation rates, increasing the avalanche time and reducing the memory on the starting angle. When the arresting front returns to the top of the drum to switch off the avalanche, it partially sets the packing there, dictating when the next avalanche begins and correlating θ_{stop} with the following θ_{start}. In the narrower drums, sidewall friction slows and weakens the arresting front so that the avalanche takes longer to terminate and the packing at the top of the drum is set by an earlier collapse, decorrelating θ_{stop} and the next θ_{start}.

4.4. *Sand spectra*

A selection of power spectra for the sand are shown in figure 25; the frequency of the dominant peak is plotted against rotation rate in figure 26. Below transition, the enhanced periodicity of episodic avalanching is highlighted by the sharpness of the main

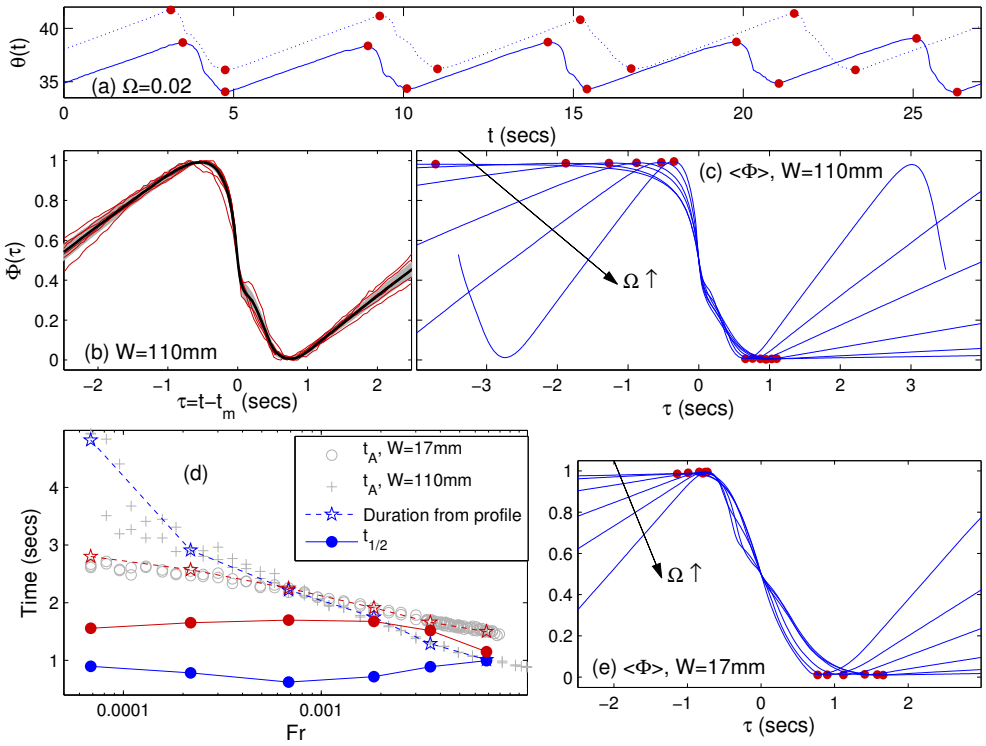

FIGURE 24. (a) Time series of surface angle for sand in the $D = 287$ mm drum with $W = 110$ mm (solid) and 17 mm (dotted). (b) Mean scaled avalanche profile for the wider drum, plus or minus the standard deviation and six sample avalanches. (c) Profiles for $W = 110$ mm at the six Froude numbers shown in panel (d), which plots the avalanche duration (time from maximum to minimum of the avalanche profile) and the characteristic time $t_{1/2}$. Blue (red) data represent the drum with $W = 287$ mm (17 mm), and the grey crosses (circles) show corresponding direct measurements of t_A. (e) Mean scaled avalanche profiles at the six Froude numbers for $W = 17$ mm.

spectral peak and the multiplicity of its harmonics. Above the transition to continuous flow, the spectra become broadly peaked and red. Strong additional peaks also appear at low frequency at the higher rotation speeds which are not connected to the motor contaminations. Direct observations of the drum indicate that these peaks correspond to coherent oscillations of the granular surface, in the manner of some sort of sloshing mode of the flowing layer. For example, at the higher speed in figure 25, $\Omega = 0.4$ rad/sec, a sloshing mode arises with a frequency of about 2.7Ω.

Figure 26 illustrates the clear switch in the dominant spectral peak when the transition is hysteretic (compare the blue and red points). For the continuous flow data plotted in this figure sloshing modes have yet to appear and the spectral peak characterizes noisy flow fluctuations. The resulting characteristic frequency is clearly distinct from that for episodic avalanching, which once more reflects the typical avalanche spacing (fits of the form (3.8) again furnish a fair representation of the data; see figure 26). Evidently, the transition arises when the slumping and rolling frequencies are well matched, much as suggested previously in some qualitative prescriptions (e.g. Henein *et al.* 1983*b*; Mellmann 2001).

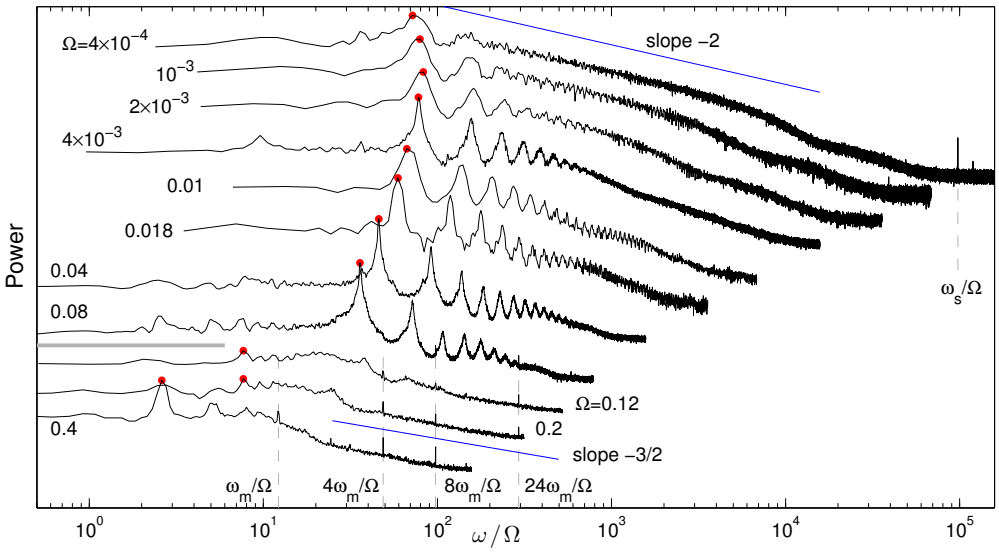

FIGURE 25. Power spectra for sand in the drum with $(D, W) = (287, 110)\,\mathrm{mm}$, plotted against ω/Ω, for the rotation rates indicated. The spectra are offset for clarity and the dominant peaks are identified. Vertical dashed lines show the additional frequencies, $\omega_s = 8000\omega_m$ and ω_m, and some of their harmonics. The transition is indicated by the grey horizontal line. The inclined dashed lines indicates slopes of -2 and $-3/2$.

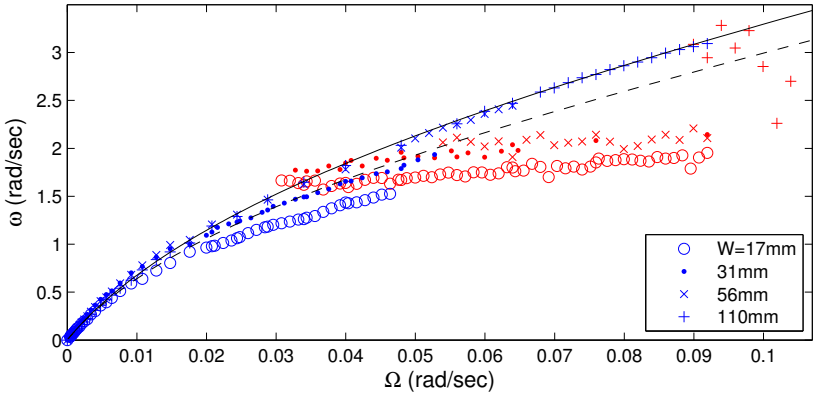

FIGURE 26. The frequency of the dominant peak in the power spectra for sand in the big drum with the widths indicated. Blue (red) symbols indicate frequencies in the episodic avalanching (continuous flow) regime. The dashed line denotes the fit in (3.8) to the $W = 110\,\mathrm{mm}$ data, using a fit to the observed t_A (figure 40) and the mean avalanche amplitude over the episodic regime $\langle\Delta\theta\rangle \approx 4^\circ$; the solid line uses least squares with (3.8), including $\Delta\theta$, t_0 and Γ as fitting parameters.

5. Conclusions

In this paper we have reported an experimental survey of the dynamics of episodic avalanching and continuous flow in a granular drum. This device is a classical arrangement to study granular dynamics, yet a detailed investigation of the two regimes and the transition between them has not previously been presented. We have tried to go some

way in this direction here, considering a variety of different granular media (glass spheres with a range of diameters and a sand) and drums with different diameters and widths. Our main advance has been to catalogue the granular dynamics over lengthy sweeps in rotation rate, afforded by an efficient data acquisition system. Sweeps could be conducted for days or even weeks on end, allowing us to collect relatively clean statistics of episodic avalanching or the vagaries of continuous flow.

For most of our spheres and drums, the transition from episodic avalanching to continuous flow takes the form of a gradual switch in dynamical behaviour wherein the two phases are blended in varying degrees. As the particle radius becomes small, the blend becomes refined into an alternation between phases of continuous flow or episodic avalanching in the manner outlined by Fischer *et al.* (2009). For sand, the transition is again intermittent in either the biggest or smallest drums, but in all others a hysteretic transition takes place (Rajchenbach 1990). Overall, the different forms of the transition are suggestive of a system in which there are two possible states and which is perturbed by differing degrees of noise. The transition is a smooth blend in behaviour for higher noise levels, hysteretic for weak noise, and intermittent in between. There is little sign that the continuous flow state disappears in some kind of a deterministic bifurcation at low rotation rates, or that episodic avalanching terminates at higher rotation rates in another bifurcation. The situation is quite different from most fluid systems in which transitions are deterministic in the absence of external stochastic perturbations, the noise here arising from intrinsic noise in the dynamics.

The results for glass spheres suggest that the transition is largely independent of drum width and arises roughly for $0.3 < \mathrm{Fr}(D/d) < 0.5$, in terms of the Froude number, $\mathrm{Fr} = \Omega\sqrt{D/g}$. This criterion is consistent with previously reported results for spheres (Brucks *et al.* 2007; Fischer *et al.* 2009), but does not work for sand which displays a more complicated dependence on the drum geometry. The criterion is different to a number of existing predictors of transition based mostly on heuristic arguments, although it is similar to one proposed by Liu *et al.* (2005) for angular particles such as sand, but not glass spheres. In any event it is hard to see how to reconcile the heuristic arguments underlying these other predictors with the nature of the transition as they take no explicit account of effect of dynamical noise. We also find little support for a suggestion by Jop *et al.* (2005) that the transition is connected to the flow-depth-surface-angle relation for sheet flow to cease on an inclined plane (see Appendix B).

Although we have resisted providing any detailed theoretical models to complement our experiments, these are certainly possible. Indeed, we conducted simulations with the Discrete Element Method in tandem with the experiments, and which helped guide some of our scalings and fits of the data. A brief discussion of a model for a relatively narrow drum based on the $mu(I)$ law is provided in Appendix B. One can also build cruder ODE models along the lines followed by Caponeri *et al.* (1995) and others. To capture the experimental observations, stochastic forcing is essential in these models. Moreover, two types of noise are needed: stochastic fluctuations in packing are required to furnish a random starting angle for an avalanche. Then dynamical noise must be added during flow to simulate fluctuations and a random stopping angle. With both types of noise suitably incorporated, models can be designed that show some qualitative agreement with the observations. However, many of the finer details (such as the distributions and

correlations of the starting and stopping angles) are likely to be awry without substantial empirical input, calling into the question the usefulness of such models.

A persistent ageing effect plagued our efforts to generate reproduceable results. We were largely successful in eliminating this feature by suitably maturing particles in high-speed burn-in experiments, and by restricting our use of glass spheres with smaller diameters. Polydispersivity may constitute another intrinsic problem, with segregation potentially also leading to long-time evolution. Overall, the surface angle during both episodic avalanching or continuous flow is sensitive to ageing effects and drum or particle geometry, and is likely to be significantly affected by external noise in less controlled situations. One should exercise caution in using such a statistic to characterise granular dynamics (cf. Kleinhans *et al.* 2011); other, more robust measures offer greater diagnostic value.

Beyond the rotating drum, one may wonder what kinds of intermittent motions occur in different flow configurations. Episodic avalanches also arise in heap flows and sandpiles fed at low flux (*e.g.* Lemieux & Durian 2000; Jop *et al.* 2005; Börzsönyi *et al.* 2008). In sheet flow down an incline (*e.g.* Forterre & Pouliquen 2008) or for bulldozed sandpiles (Sauret *et al.* 2014), however, episodic avalanching does not occur at low flow rates. For the inclined plane, fluctuations during continuous flow trigger the arrest of flow, but once the grains stop noise cannot drive the system back into motion, precluding any recurring slumping state. For the bulldozer, there is again a continuous flow state, but the driving appears to preclude any locked-up arrangement like rigid rotation. Stochastic fluctuations can then only agitate the system about the continuous flow state. The rotating drum has the relatively unique feature that a truly rigid phase can emerge over long intervals, but not persist indefinitely.

We thank Greg Wagner and Quentin Debray for assistance and discussions.

REFERENCES

Börzsönyi, T, Halsey, TC & Ecke, RE 2008 Avalanche dynamics on a rough inclined plane. *Physical Review E* **78** (1), 011306.

Brucks, A, Arndt, T, Ottino, JM & Lueptow, RM 2007 Behavior of flowing granular materials under variable g. *Physical Review E* **75** (3), 032301.

Caponeri, M, Douady, S, Fauve, S & Laroche, C 1995 Dynamics of avalanches in a rotating cylinder. In *Mobile particulate systems*, pp. 331–366. Springer.

Courrech du Pont, S, Gondret, P, Perrin, B & Rabaud, M 2003*a* Granular avalanches in fluids. *Physical review letters* **90** (4), 044301.

Courrech du Pont, S, Gondret, P, Perrin, B & Rabaud, M 2003*b* Wall effects on granular heap stability. *EPL (Europhysics Letters)* **61** (4), 492.

Davidson, J, Scott, D, Bird, P, Herbert, O, Powell, A & Ramsay, H 2000 Granular motion in a rotary kiln: the transition from avalanching to rolling. *KONA Powder and Particle Journal* **18** (0), 149–156.

Ding, YL, Forster, R, Seville, JPK & Parker, DJ 2002 Granular motion in rotating drums: bed turnover time and slumping–rolling transition. *Powder Technology* **124** (1), 18–27.

Dury, CM, Ristow, GH, Moss, JL & Nakagawa, M 1998 Boundary effects on the angle of repose in rotating cylinders. *Physical Review E* **57** (4), 4491.

Félix, G, Falk, V & D'Ortona, U 2007 Granular flows in a rotating drum: the scaling law between velocity and thickness of the flow. *The European Physical Journal E: Soft Matter and Biological Physics* **22** (1), 25–31.

Fischer, R., Gondret, P., Perrin, B. & Rabaud, M. 2008 Dynamics of dry granular avalanches. *Physical Review E* **78** (2), 021302.

Fischer, R, Gondret, P & Rabaud, M 2009 Transition by intermittency in granular matter: from discontinuous avalanches to continuous flow. *Physical review letters* **103** (12), 128002.

Forterre, Y & Pouliquen, O 2008 Flows of dense granular media. *Annu. Rev. Fluid Mech.* **40**, 1–24.

GDR MiDi 2004 On dense granular flows. *Eur. Phys. J. E* **14**, 341–365.

Henein, H, Brimacombe, JK & Watkinson, AP 1983*a* Experimental study of transverse bed motion in rotary kilns. *Metallurgical transactions B* **14** (2), 191–205.

Henein, H, Brimacombe, JK & Watkinson, AP 1983*b* Modelling of transverse solids motion in rotary kilns. *Metallurgical transactions B* **14** (2), 207–220.

Jenkins, James T & Berzi, Diego 2010 Dense inclined flows of inelastic spheres: tests of an extension of kinetic theory. *Granular Matter* **12** (2), 151–158.

Jop, P, Forterre, Y & Pouliquen, O 2005 Crucial role of sidewalls in granular surface flows: consequences for the rheology. *Journal of Fluid Mechanics* **541**, 167–192.

Kleinhans, MG, Markies, H, De Vet, SJ, Postema, FN *et al.* 2011 Static and dynamic angles of repose in loose granular materials under reduced gravity. *Journal of Geophysical Research: Planets (1991–2012)* **116** (E11).

Lemieux, P-A & Durian, DJ 2000 From avalanches to fluid flow: a continuous picture of grain dynamics down a heap. *Physical review letters* **85** (20), 4273.

Lim, S-Y, Davidson, JF, Forster, RN, Parker, DJ, Scott, DM & Seville, JPK 2003 Avalanching of granular material in a horizontal slowly rotating cylinder: Pept studies. *Powder technology* **138** (1), 25–30.

Liu, XY, Specht, E & Mellmann, J 2005 Slumping–rolling transition of granular solids in rotary kilns. *Chemical engineering science* **60** (13), 3629–3636.

Maneval, JE, Hill, KM, Smith, BE, Caprihan, A & Fukushima, E 2005 Effects of end wall friction in rotating cylinder granular flow experiments. *Granular Matter* **7** (4), 199–202.

Mellmann, J 2001 The transverse motion of solids in rotating cylindersforms of motion and transition behavior. *Powder Technology* **118** (3), 251–270.

Orpe, AV & Khakhar, DV 2007 Rheology of surface granular flows. *Journal of Fluid Mechanics* **571**, 1–32.

Pouliquen, O & Forterre, Y 2002 Friction law for dense granular flows: application to the motion of a mass down a rough inclined plane. *Journal of Fluid Mechanics* **453**, 133–151.

Rajchenbach, J 1990 Flow in powders: From discrete avalanches to continuous regime. *Physical review letters* **65** (18), 2221.

Rajchenbach, J 2000 Granular flows. *Advances in Physics* **49** (2), 229–256.

Rajchenbach, J 2002 Dynamics of grain avalanches. *Physical review letters* **88** (1), 014301.

Sauret, A, Balmforth, NJ, Caulfield, CP & McElwaine, JN 2014 Bulldozing of granular material. *Journal of Fluid Mechanics* **748**, 143–174.

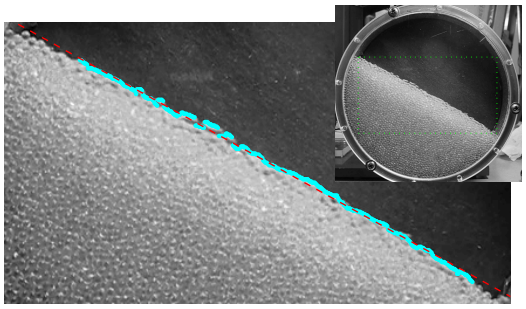

FIGURE 27. An image taken of the 2mm spheres in the 137mm diameter drum ($W = 17\,\mathrm{mm}$), together with the extraction of the surface profile and its linear fit.

Appendix A. Experimental details

A.1. *The motor for the bigger drum*

The larger cylinder was driven by a high performance stepper motor (a Parker Compumotor iBE342H), which could rotate stably very low speeds. Given that the dynamics of episodic avalanching could potentially be sensitive to variations in motor speed we estimated the precision of this device by monitoring time series of the angular position of the shaft. In its velocity-controlled mode, the motor has settings to improve speed stability; using suitable choices for these (in the Parker nomenclature, we used KI= 0, KP= 10 and KD= 1000, for the integral, proportionality and damping constants, respectively), the angular position error was always less than 0.06 degrees over the duration of each experiment. However, velocity fluctuations do occur during each run as the motor adjusts to maintain the angular position. The inertia and compliance of the drum apparatus likely lessen these variations, but our best estimates suggested that rotation rate errors of order 5×10^{-5} rad/sec could occur over intervals of several seconds. These errors are somewhat lower than the smallest rotation rates used, but the associated accelerations may contribute to the ambient agitation of the apparatus and trigger avalanches.

A.2. *Image processing*

Image processing was performed in real time, mostly at 20 Hz, for the central section of the drum, excluding the first and last two centimetres of the surface. The surface was identified by finding the highest pixel in each vertical raster that was above a threshold intensity set to be halfway between the raster's minimum and maximum. The best fit straight line to the identified pixels was then found and all points lying at least ten pixels from the fit were then marked as outliers; discarding those outliers, the line was fit a second time and any new outliers again discarded. Repeating the procedure one more time furnished the slope angle (the dynamic friction angle, $\theta(t)$) and well as its vertical offset. An example is shown in figure 27. The procedure does not therefore fit the entire surface profile, and is misleading when the drum is rotating relatively quickly and the characteristic S-shape develops. As diagnostics of the goodness of fit, we recorded the mean squared error and the fraction of discarded points (which was typically less than 5%). We also constructed average images and the differences between successive images in order to furnish mean surface profiles and examine the apparent flowing layer depth.

Although the surface is relatively flat for most of our experiments, the profile becomes

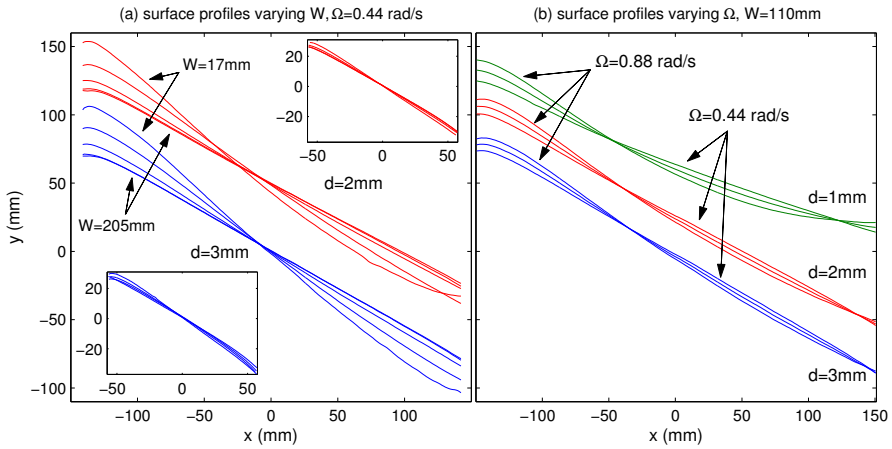

FIGURE 28. (a) Surface profiles for the drum with $D = 289\,\text{mm}$ and varying width, filled with 2 mm (red, vertically offset) and 3 mm (blue) spheres. The insets show the same data, but for the drum with $D = 137\,\text{mm}$. (b) Surface profiles for particles with diameter $d = 1$, 2 and 3 mm, in the drum with $(D, W) = (287, 110)\,\text{mm}$, for $\Omega = 0.44$, 0.66 and 0.88 rad/sec.

nonlinear as the drum is rotated more quickly and its width is reduced. Figure 28 displays mean surface profiles for the fastest drums. The characteristic S-shape develops at these speeds, becoming most prominent for the biggest diameter, narrowest drums and the smallest particles. Note that the surface profiles in the two widest drums ($W = 110$ and 205 mm) are practically identical, indicating that the dynamics is insensitive to the width for these cases, yet the S-shape still develops.

For each time series of $\theta(t)$, the initial 10 seconds or longer were clipped to remove transients. A median filter over a width of 5 samples was then applied to reduce noise. The starting and stopping angles, θ_{start} and θ_{stop}, were identified by first calculating the standard deviation σ of $\theta(t)$. For a time series with a periodic triangular waveform of peak-to-peak amplitude $\Delta\theta$, the distribution of θ is uniform and $\sigma = \Delta\theta/\sqrt{12}$. We therefore chose an angle threshold $\delta_\theta = \frac{1}{5}\Theta/\sqrt{12}$ designed to detect avalanches of amplitude down to about 1/5 of the average. If the avalanche time is much less that the time for solid-body rotation, this corresponds to a time interval between avalanches of $\delta_t = \delta_\theta/\omega$. The moving maximum over θ corresponding to this time interval is then found and the start of each avalanche identified as the times where θ equals this maximum. We then find all the minimum values between each pair of maxima to locate the end of each avalanche. Finally the candidate list of avalanches is searched and any that are smaller than δ_θ are removed. The procedure is robust and copes well with noisy signals, but clips the smallest avalanches.

Given the time series $\theta(t_i) = \theta_i$ (t_i being the i^{th} sampling time), we may define the distance skewness of the rate of change $\dot{\theta}_i = (\theta_{i+k} - \theta_i)/(t_{i+k} - t_i)$, by

$$D_{skew}(t_k) = 1 - \frac{\sum_{i,j} |\dot{\theta}_i - \dot{\theta}_j|}{\sum_{i,j} |\dot{\theta}_i + \dot{\theta}_j|},$$

for a prescribed delay time t_k. For each time series we optimised the choice for the delay

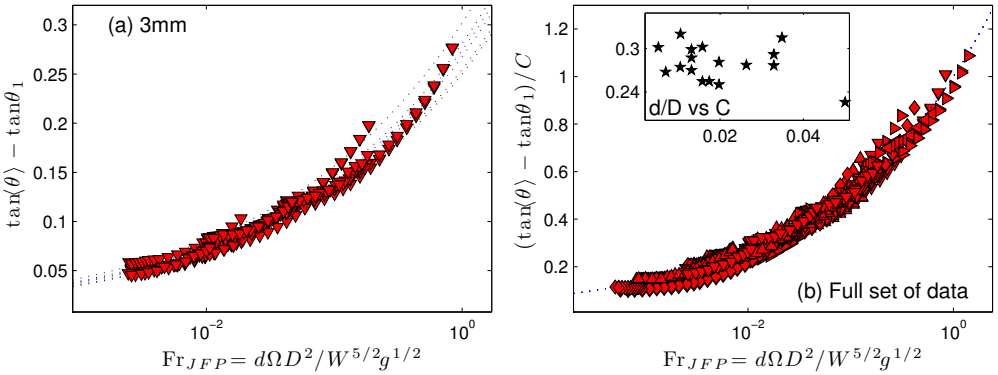

FIGURE 29. (a) Mean angle data in continuous flow ($D_{skew} < 0.01$) for 3mm glass spheres in the narrower drums, $3W < D$, plotting $\tan\langle\theta\rangle - \tan\theta_1$ against $\mathrm{Fr}_{JFP} = d\Omega D^2/\sqrt{gW^5}$, where $\tan\theta_1$ is the intercept determined from a linear fit of $\tan\langle\theta\rangle$ to $\mathrm{Fr}_{JFP}^{2/7}$, (dotted lines). (b) Mean angles for glass spheres, plotting $(\tan\langle\theta\rangle - \tan\theta_1)/C$ against Fr_{JFP}, where C is the slope of the linear fits. The symbol convention follows the legend of figure 6. The inset plots C against d/D.

time t_k by increasing k until D_{skew} reached a maximum, and then adopted the maximal value.

Appendix B. A mu(I) interlude

A different representation of the continuous flow data for the narrower drums ($3W < D$) is shown in figure 29, which plots mean surface slopes against the scaled Froude number $\mathrm{Fr}_{JFP} = \Omega d D^2/W^{5/2}\sqrt{g}$. This unobvious scaling of the mean slope data is suggested by a simple model based on the mu(I) law, much as Jop *et al.* (2005) rationalized data for heap-flow experiments. The essential idea is to consider a shallow flowing layer of depth $\delta \ll R$ inclined at angle $\langle\theta\rangle$ with respect to gravity and confined within a narrow slot. As shown by Jop *et al.*, one can compute the flow depth and flux if the $mu(I)-$law is expressed as

$$\mu(I) = \frac{I_0\mu_1 + I\mu_2}{I_0 + I} \tag{B 1}$$

where μ_1, μ_2 and I_0 are material parameters. The flowing layer depth is

$$\delta = \frac{W}{\mu_w}(\tan\langle\theta\rangle - \mu_1), \tag{B 2}$$

where μ_w is the coefficient of sliding friction over the walls, and the net flux is

$$q = 2I_0\frac{\sqrt{g\cos\langle\theta\rangle}}{5d}\left[W\frac{(\mu_2-\mu_1)}{\mu_w}\right]^{5/2} F\left(\mu_w\frac{\delta W^{-1}}{\mu_2} - \mu_1\right), \tag{B 3}$$

where

$$F(X) = 5(1-X)\left[\sqrt{1-X}\sin^{-1}\sqrt{X} - \sqrt{X}\right] + \frac{5}{3}X^{3/2} - X^{5/2}. \tag{B 4}$$

For the drum, the flux through the flowing layer at drum centre must match the influx by rotation: $q = \frac{1}{8}\Omega D^2$. Hence (B 3) boils down an algebraic equation for θ given the rotation rate (and other parameters). The full algebraic form of (B 4) is a little unwieldy and its value is not so different over the simpler, small X approximation, $F \approx \frac{2}{7}X^{7/2}$.

We therefore adopt the latter as a more useful approximation, in which case we find

$$\tan\theta = \mu_1 + \left(\frac{\mu_w}{W}\right)^{5/7}\left[\frac{35dR^2\Omega(\mu_2-\mu_1)}{8I_0\sqrt{g\cos\langle\theta\rangle}}\right]^{2/7}. \qquad \text{(B 5)}$$

This relates $\tan\langle\theta\rangle - \mu_1$ to Fr_{JFP}, as plotted in figure 29, and is equivalent to the scaling of heap-flow data by Jop, Forterre & Pouliquen (2005; their fig 11). For the lower rotation rates, the data bend away from the prediction, reflecting the impending transition to episodic avalanching. At the higher rotation speeds, the data again bend away from the data, possibly due to inertia (the approximation of $F(X)$ is not responsible). The limiting friction μ_1 and the factor $\mu_w^{5/7}[35(\mu_2-\mu_1)/8I_0\sqrt{\cos\langle\theta\rangle}]^{2/7}$ provide interpretations of the intercept $\tan\theta_1$ and slope C of the fits in figure 29.

Jop *et al.* suggest that episodic avalanching begins when the flow-depth-flux relation intersects the $h_{stop}(\langle\theta\rangle)$ curve for sheet flow down an inclined plane (*i.e.* the depth-angle relation holding when flow ceases on reducing the incline). Because we have not measured h_{stop}-curves for our spheres, we cannot directly examine this supposition. However, near the onset of flow, one expects that $h_{stop} \propto d(\tan\langle\theta\rangle - \mu_1)^{-m}$, with $m \approx 1$, from empirical determinations of this curve (e.g. Pouliquen & Forterre 2002). Thus, setting $\delta \sim d(\tan\langle\theta\rangle - \mu_1)^{-m}$, or $\delta \sim W(d/W)^{1/(m+1)}$, suggests that the critical Froude number for transition scales as $\mathrm{Fr} \sim W^{(5m-2)/2(m+1)}d^{(5-2m)/2(m+1)}/D^{3/2}$. This is only consistent with the relatively weak dependence of Fr^{upper} in (3.2) on W if $m = 2/5$. However, the transitional Froude number then scales as $\mathrm{Fr} \sim (d/D)^{3/2}$, in poor agreement with (3.2).

For the wider drum, no equivalent theory exists to predict the depth of the flowing layer or flux from $mu(I)$. Nevertheless, assuming that the inertia number plays a key role, we may dimensionally estimate an average,

$$I \sim \frac{qd}{\delta^2\sqrt{g\delta}} \equiv \frac{dD^2\Omega}{8\delta^2\sqrt{g\delta}}, \qquad \text{or} \qquad \frac{\delta}{d} \sim \left(\frac{\mathrm{Fr}}{I}\right)^{2/5}\left(\frac{D}{d}\right)^{3/5}. \qquad \text{(B 6)}$$

If the average I is roughly constant, the estimate for δ/d is not far from the scaling $(\delta/d) \sim \sqrt{\mathrm{Fr}}(D/d)^{3/4}$ reported in GDR-MiDi (2004). Our fit of the mean angle data in (3.4) suggests that C depends weakly on particle radius in relatvely wide drums. In this case, Jop *et al.*'s strategy for locating transition furnishes a scaling, $\mathrm{Fr} \sim (d/D)^{3/(2+5m)}$. If $m = 1$ or $2/5$, the Froude number scales as either $(d/D)^{3/7}$ or $(d/D)^{3/4}$, neither of which compares particularly well with (3.2) for $\alpha \approx 1.1$ and $\beta d/W \to 0$.

We conclude that the mean angle scalings suggested by the thin-slot $mu(I)$ model are consistent with the drum data to a similar degree that Jop *et al.* account for their heap flow experiments. Our observed transition, however, does not appear to coincide with a criterion based on $h_{stop}(\langle\theta\rangle)$.

Appendix C. Synthetic avalanche spectra

We construct synthetic time series of the surface angle as illustrated in figure 30(a): we randomly choose a sequence of values for the starting and stopping angles and the avalanche durations from Gaussian distributions. The signal is then built by adopting a linear rise at the rotation rate between a given stopping angle and the following starting

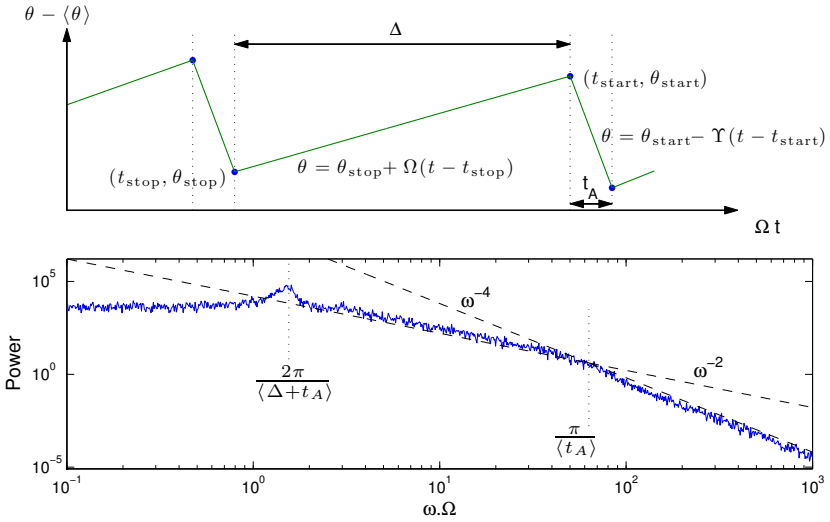

FIGURE 30. (a) Synthetic time series of the surface angle constructed from random variables representing the starting and stopping angles, $\theta_{\rm start}$ and $\theta_{\rm stop}$, and the duration of the avalanches, t_A. (b) average power spectrum from ten realizations of the synthetic time series, based on $N = 2000$ avalanches. $\theta_{\rm start}$ and $\theta_{\rm stop}$ are chosen from Gaussian distributions with means separated by $\langle \Delta\theta \rangle = 4$ and standard deviations of 0.5, and Ωt_A selected from a Gaussian distribution with mean 0.05 and standard deviation 0.0125.

angle, then inserting a linear collapse of duration t_A to the next stopping angle. The time series for a realization of N avalanches can be used to compute spectra, as illustrated in figure 30(b), either by exploiting a fast Fourier transform or by explicitly evaluating the coefficients of its Fourier series.

The mean and standard deviation of the signal of $\theta(t)$ can be computed analytically in terms of the statistics of the random variables, after evaluating the time integrals and replacing the sum over avalanches by expectations. One finds

$$\langle \theta(t) \rangle = \frac{1}{2}\langle \theta_{\rm start} + \theta_{\rm stop} \rangle \left[1 + \frac{\sigma^2_{\rm start} - \sigma^2_{\rm stop}}{\langle \theta_{\rm start} + \theta_{\rm stop} \rangle \langle \theta_{\rm start} - \theta_{\rm stop} + \Omega t_A \rangle} \right] \tag{C 1}$$

and

$$\sigma^2 = \frac{1}{12}\langle \theta_{\rm start} - \theta_{\rm stop} \rangle^2 + \frac{1}{2}(\sigma^2_{\rm start} + \sigma^2_{\rm stop}) \frac{\langle \theta_{\rm start} - \theta_{\rm stop} + \frac{2}{3}\Omega t_A \rangle}{\langle \theta_{\rm start} - \theta_{\rm stop} + \Omega t_A \rangle} - \frac{(\sigma^2_{\rm start} - \sigma^2_{\rm stop})^2}{4\langle \theta_{\rm start} - \theta_{\rm stop} + \Omega t_A \rangle^2}. \tag{C 2}$$

Appendix D. Additional results

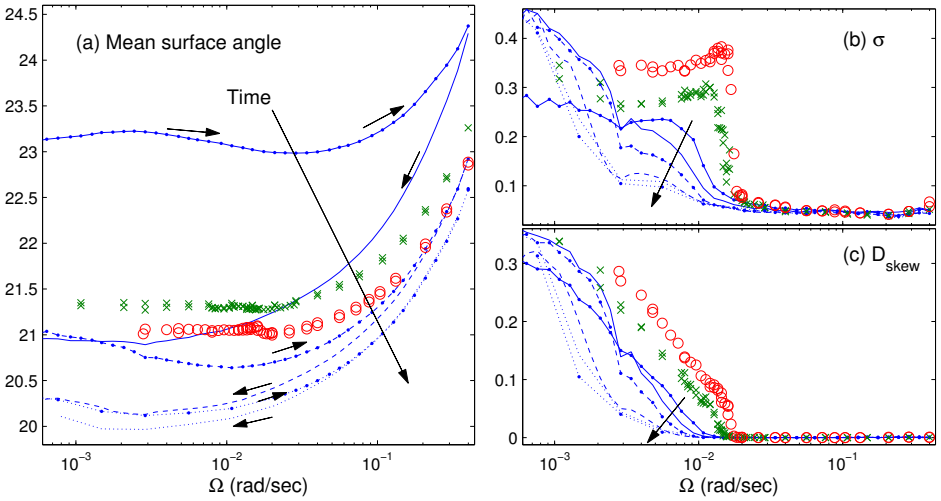

FIGURE 31. Repeated sweeps conducted with a fresh sample of 1 mm spheres in a drum with $(D, W) = (287, 110)$mm, showing (a) the secular decrease of the mean surface angle $\langle\theta(t)\rangle$, (b) the standard deviation σ, and (c) the distance skewness D_{skew}. The repeated sweeps are shown by lines (in the up/down repeated sequence dots/solid, solid, dots/dashed, dashed, dots/dotted, dotted); the angle change is over twice that for $d = 3$mm shown in figure 1 of the main text. The circles and crosses show two up-down sweeps for spheres that were matured as follows: the spheres were aged in a first burn-in run, then removed from the drum and washed, and finally aged in a burn-in run (see figure 32). The slumping-to-rolling transition then becomes more robust but the results are still not especially reproducible, with significant discrepancies arising between the two batches of similarly prepared particles.

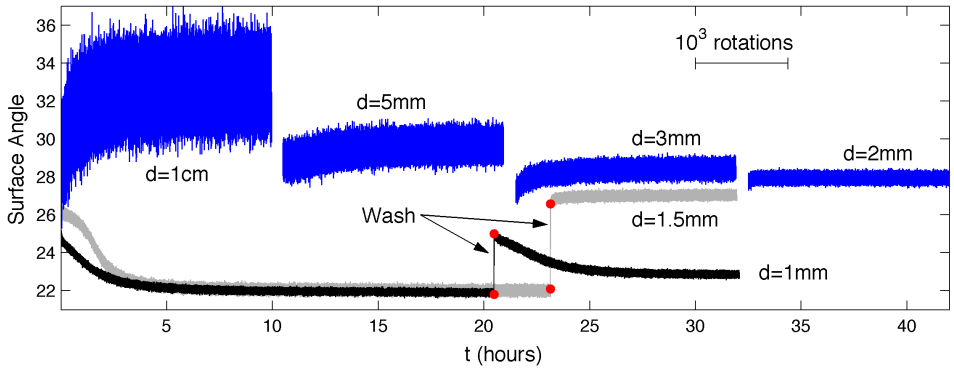

FIGURE 32. Burn-in runs, showing the drift of the surface angle at fixed speed (0.4 rad/sec) for the glass spheres indicated in the $(D, W) = (287, 110)$mm drum. The upward shift of the mean angle is evident for the spheres with diameter $d > 2$ mm. For $d = 2$ mm, there is barely any drift; the 1.5 and 1 mm particles both drift downward. For 1.5 mm and 1mm spheres, the material is washed after the first burn, and then aged a second time. For the 1.5 mm, the washing of the particles reverses the sense of the drift during the second burn-in, with the mean angle then increasing. To display the data without any overlap, some of the time traces are shifted horizontally.

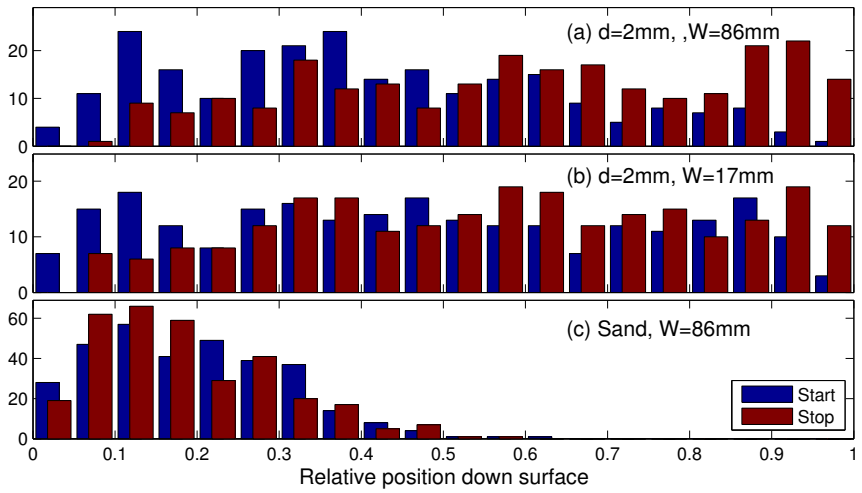

FIGURE 33. Histograms of the relative starting and stopping positions of avalanches down the granular surface (defined so that 0 refers to the top of the inclined surface and 1 to the bottom in the image taken by the video camera) for $d = 2\,\mathrm{mm}$ glass spheres and sand in the drum with $D = 137\,\mathrm{mm}$ and the widths indicated. The position is determined by locating the pixels of the first or last coherent motions away from rigid rotation (discarding individual grain motion), or by taking the average of such positions if multiple locations are indistinguishable.

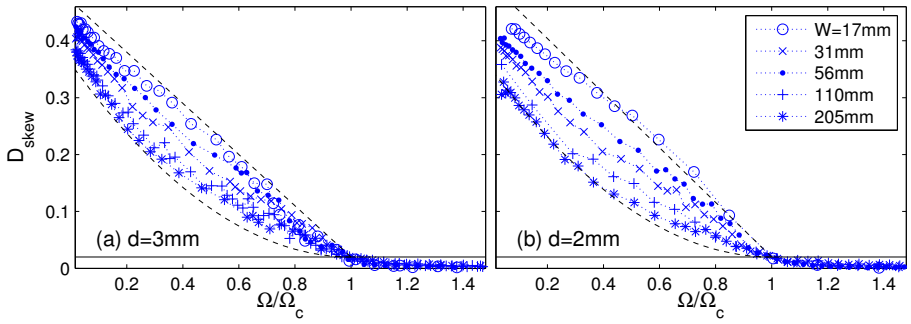

FIGURE 34. D_{skew} plotted against Ω/Ω_c for (a) $d = 3\,\mathrm{mm}$ and (b) $d = 2\,\mathrm{mm}$ spheres from the larger drum ($D = 289\,\mathrm{mm}$), with the different symbols corresponding to the widths indicated. As in figure 6, Ω_c is the interpolated rotation rate for which $D_{skew} = D_{crit} = 0.02$ (this threshold is also indicated). The diagnostic increases more sharply in the narrower drums than the wider ones as episodic avalanching commences; the dashed lines show the fits, $D_{skew} \propto (1 - \Omega/\Omega_c)$ and $D_{skew} \propto (1 - \Omega/\Omega_c)^{3/2}$. Note that the observed D_{skew} do not abruptly reduce to zero but trail off gradually as one passes through $\Omega = \Omega_c$, much as in an imperfect bifurcation.

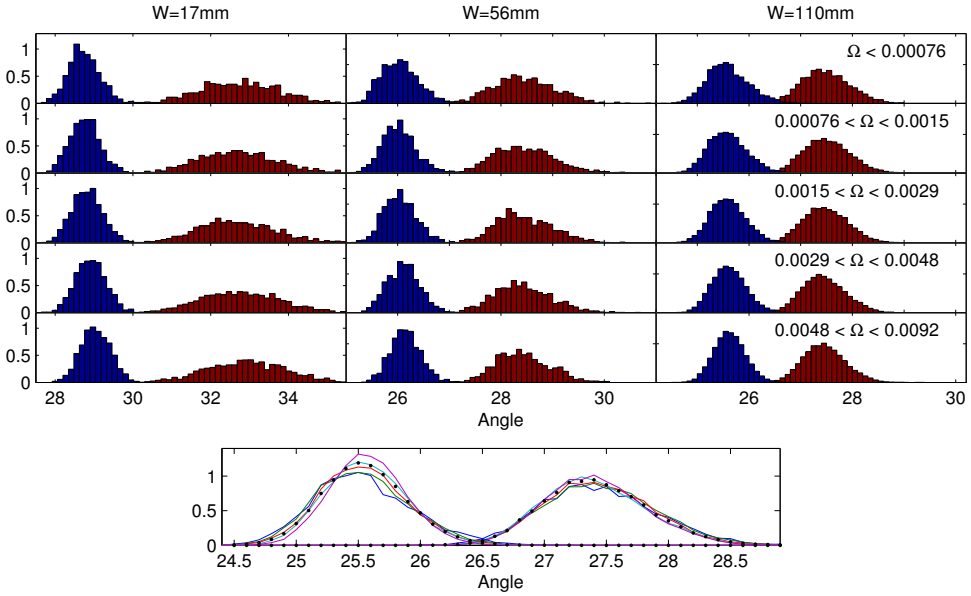

FIGURE 35. Histograms of $\theta_{\rm start}$ and $\theta_{\rm stop}$ for $d = 3\,$mm spheres in the drum with $D = 287$mm and the widths and rotation rates indicated. The final panel compares the distributions for $(D, W) = (287, 110)$mm; the dots show the average over the slumping regime.

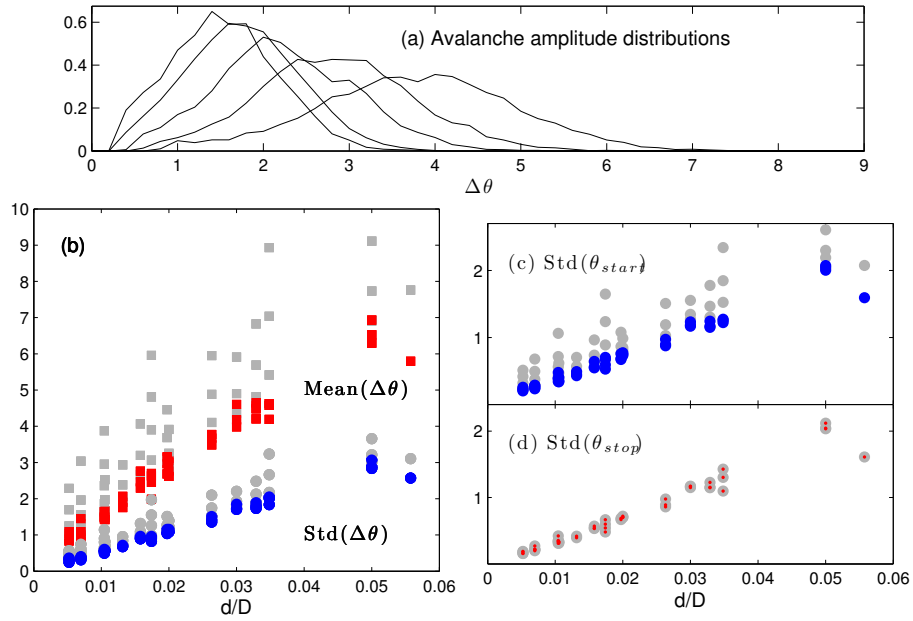

FIGURE 36. (a) Avalanche amplitude distributions for $(d, D) = (3, 287)$mm and $W = 17$, 31, 56, 110 amd 205mm (as shown in figure 10). (b) The mean and standard deviation of the distribution as a function of d/D; grey points show the raw data, the darker (red and blue) points after the drum width dependence is removed using a linear fit with d/W. (c)–(d) The standard deviation of the $\theta_{\rm start}$ and $\theta_{\rm stop}$ distributions. Std($\theta_{\rm stop}$) shows no significant dependence on drum width; the drum width dependence of Std($\Delta\theta$) therefore originates purely from that of $\theta_{\rm start}$.

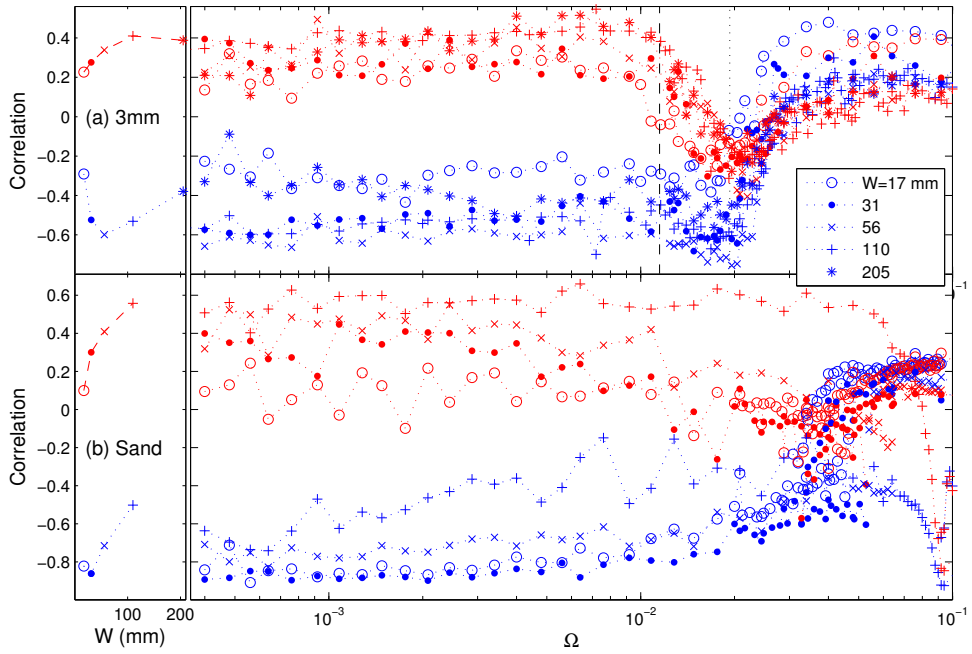

FIGURE 37. Correlation coefficients between $\theta_{\rm start}$ and the following $\theta_{\rm stop}$ (blue) and the previous $\theta_{\rm stop}$ (red) plotted against Ω for (a) 3 mm spheres and (b) sand in the big drum. Each data point is averaged over all experiments at the same rotation rate; for the hysteretic sand data, the averages are taken only over experiments with the same phase. The symbols refer to drum width, as indicated. The panels on the left show averages for $\Omega < 0.01$, plotted against W, In (a), the vertical dotted and dashed lines indicate the upper and lower edges of the transition region, ignoring the weak width-dependence.

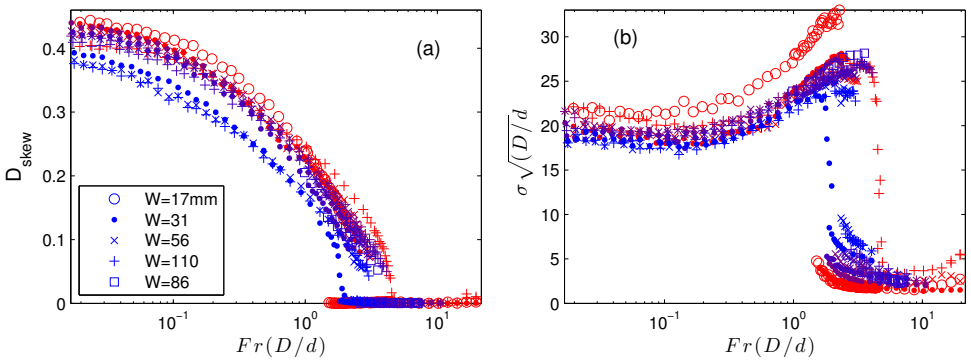

FIGURE 38. (a) D_{skew} and (d) σ for sand, scaled as indicated and plotted against $\mathrm{Fr}(D/d)$, which collapses the data close to a common curve. Each data point is an average over all experiments with the same (Ω, D, W) and phase (episodic avalanching or continuous flow), and the points are colour coded according to drum diameter (red for $D = 100$mm and blue for $D = 287$mm). The plot conveys the impression that statistics of episodic avalanching are largely independent of W, but the transition to continuous flow takes place at a width-dependent Froude number.

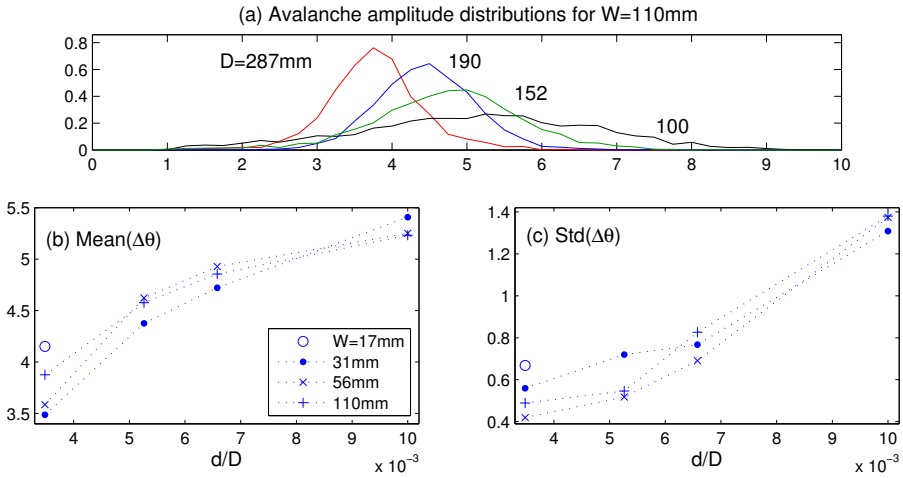

FIGURE 39. (a) Avalanche amplitude distributions for sand in the drum with varying D and $W = 110$mm. The mean and standard deviation of these distributions are plotted in (b) and (c), respectively. The distributions, means and standard deviations show no clear trend with drum width, unlike the glass spheres (*cf.* figure 36).

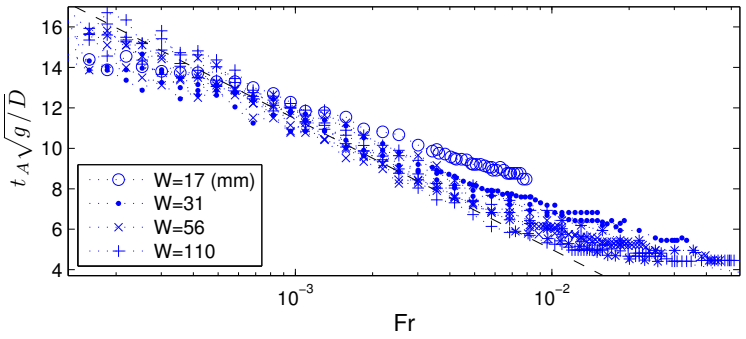

FIGURE 40. Median avalanche times, scaled by $\sqrt{g/D}$, against Froude number for sand. The dashed line is the linear fit to the $(D, W) = (287, 110)$ mm data used in figure 26.